

# A Search for Metal-Poor Stars in the Halo of the Milky Way

Aruba Mohammed



Physics

Department of Physics

Lancaster University

17/10/2022

A thesis submitted to Lancaster University for the degree of  
Master's by Research in the Faculty of Science and Technology

*Supervised by Dr Brooke Simmons and Dr David Sobral*

## **Acknowledgements**

This thesis would not have been possible without the encouraging words of my supervisors, friends and family. Particularly, I would like to thank Dr Brooke Simmons and Dr David Sobral for their continuing support, and for providing me with the opportunity to explore and complete this investigation.

I would also like to thank Ted Maw, Tom Cornish and Heather Wade in helping me understand PYTHON and the science more so I was able to complete my project.

## **Declaration**

This thesis is my own work and no portion of the work referred to in this thesis has been submitted in support of an application for another degree or qualification at this or any other institute of learning.

# Contents

<b>List of Figures</b>	<b>vi</b>
<b>1 Introduction</b>	<b>2</b>
1.1 Characteristics of Stars . . . . .	2
1.1.1 Metallicity . . . . .	3
1.1.1.1 Nomenclature . . . . .	3
1.1.2 Luminosity, Flux and Magnitudes . . . . .	4
1.1.3 Filters and Magnitude Systems . . . . .	4
1.1.4 Temperature and Blackbody Radiation . . . . .	6
1.1.5 Mass . . . . .	7
1.2 Using Stellar Characteristics to Classify Stars . . . . .	8
1.2.1 Spectroscopy . . . . .	8
1.2.1.1 Balmer Lines Leading to OBAFGKM . . . . .	8
1.2.1.2 CaHK Absorption Lines . . . . .	9
1.2.2 Hertzsprung-Russell Diagrams . . . . .	10
1.3 Stellar Formation and Populations of Stars . . . . .	13
1.3.1 Star Formation . . . . .	13
1.3.2 First Stars . . . . .	14
1.3.3 What Spectral Type Will the Low-Mass Pop III Survivors be? . . . . .	14
1.3.4 Formation of Population I and II Stars . . . . .	15
1.3.5 Properties of Population I and II Stars . . . . .	15
1.4 The Initial Mass Function . . . . .	16
1.4.1 Metallicity Distribution Function . . . . .	17

---

1.5	Metal-Poor Stars . . . . .	18
1.5.1	Techniques to search for metal-poor stars . . . . .	19
1.5.1.1	Proper-Motion-Based Searches . . . . .	20
1.5.1.2	Objective-Prism Surveys . . . . .	20
1.5.1.3	Spectroscopic Surveys . . . . .	20
1.5.1.4	Photometric Surveys . . . . .	21
1.6	Motivations and COSMOS . . . . .	21
<b>2</b>	<b>Catalogue and Data</b>	<b>23</b>
<b>3</b>	<b>Identifying potential metal-poor candidates</b>	<b>25</b>
3.1	Catalogue Matching . . . . .	25
3.2	Limiting Magnitude . . . . .	26
3.3	Star-Galaxy Cut . . . . .	26
3.4	Errors . . . . .	29
3.5	CLASS_STAR . . . . .	31
<b>4</b>	<b>Final Candidates</b>	<b>33</b>
4.1	Visual Inspection . . . . .	33
<b>5</b>	<b>Using simulated stellar spectra to estimate metallicities</b>	<b>36</b>
5.1	Calculating Magnitudes . . . . .	36
5.2	Correlation Between g-i and Temperature . . . . .	39
5.3	Colour-Colour Plots . . . . .	44
5.4	Metallicity Heatmap . . . . .	46
5.4.1	Approximating uncertainties on metallicities . . . . .	48
<b>6</b>	<b>Number Densities and Distance Estimates of Metal-Poor Stars</b>	<b>49</b>
6.1	Number Densities . . . . .	49
6.1.1	Expected Number Densities of EMP and UMP Stars . . . . .	53
6.2	Estimated Stellar Distances . . . . .	54
<b>7</b>	<b>Metallicity Distributions</b>	<b>58</b>

<b>8</b>	<b>Future work</b>	<b>60</b>
<b>9</b>	<b>Conclusions</b>	<b>62</b>
	<b>Appendix A Appendices</b>	<b>64</b>
	A.1 Completeness and Contamination . . . . .	64
	A.2 165 candidates summary . . . . .	65
	<b>References</b>	<b>72</b>

# List of Figures

1.1	The transmission profiles of the filters used in this study <i>NB392</i> , <i>u</i> , <i>g</i> , and <i>i</i> . . . . .	5
1.2	Diagram representing how blackbody radiation changes with temperature taken from Libretexts (2022). . . . .	7
1.3	A diagram showing the different spectral classes with their specific temperatures (Gotame, 2020). . . . .	9
1.4	A demonstration of how the CaHK absorption can vary in relation to metallicity for a G-type star sourced from the Pollux database. . . . .	10
1.5	A Hertzsprung-Russell Diagram taken from Universe today showing the different regions such as the main sequence and red giants (Johnston, 2022). . . . .	11
1.6	Visible part of the solar spectrum with the Fraunhofer absorption lines indicated (Commons, 2022). . . . .	16
3.1	A histogram of NB392 magnitudes for the RUBY catalogue with a line showing the limiting magnitude to be 25. . . . .	26
3.2	A sample of potential stars and galaxies separated using the magnitude differences $U - J$ vs $J - K$ . . . . .	28
3.3	The catalogue of sources after removing the galaxies identified by a star-galaxy cut. . . . .	29
3.4	A histogram of the errors in $g - i$ ( $\sigma_x$ ) for the 9871 sources with the limiting error indicated to be 0.20. . . . .	30
3.5	A histogram of the errors in $NB392 - g - (g - i)$ ( $\sigma_y$ ) for the 9871 sources with the limiting error indicated to be 0.35. . . . .	30

3.6	A histogram of CLASS_STAR for the 2633 showing there is a clear separation between galaxies and stars. Anything above 0.97 was considered to be a star and used to create a subset of candidate that were ready for visual inspection. . . . .	31
4.1	High resolution ACS images of a sample of candidates identified as galaxies/non-stars. The images were taken from NASA/IPAC Infrared Science Archive and have a size of $15'' \times 15''$ . . . . .	34
4.2	High resolution ACS images of a sample of candidates identified as stars. The images were taken from NASA/IPAC Infrared Science Archive and have a size of $15'' \times 15''$ . . . . .	35
5.1	A plot of the temperature of the 102 synthetic spectra vs their $g-i$ colour to show the correlation between the two parameters fitted with a curve of best fit described by the fourth-order polynomial shown in equation 6.3. . . . .	40
5.2	Plots of the reduced $\chi^2$ AIC and BIC values vs polynomial order with 5.2d showing a zoomed in version of the BIC plot to show that the optimal order of polynomial is 4. . . . .	41
5.3	A colour-colour plot illustrating the separation between metallicities of 102 AFKM synthetic spectra from POLLUX that each have integer metallicities 0 to -5. The axes are $NB392 - u - (g - i)$ vs $g - i$ . . . . .	44
5.4	A colour-colour plot illustrating the separation between metallicities of AFGK synthetic spectra from POLLUX that each have integer metallicities 0 to -5. The axes are $NB392 - g - (g - i)$ vs $g - i$ . . . . .	45
5.5	Plots of the metallicity heatmap without and with candidate metal-poor stars. . . . .	47
6.1	A visual representation of the information displayed in Table 6.2 which are the number densities per spectral type for each metallicity. . . . .	51
7.1	Metallicity distribution function for F, G and K type stars identified from the 165 metal-poor candidates . . . . .	59

## Abstract

Metal-poor stars are essential in developing an understanding of the nature of the early Universe and the first stars.

This study is based on the investigation by Jenkins et al. (2019), which used the data that Sobral et al. (2017) gathered from the COSMOS field using the Isaac Newton Telescope (INT) between 2013 and 2015, for the CALYMHA survey. The catalogue contained 123,505 sources and the aim of the investigation was to discover Pop III stars or their direct descendants.

The goal of this research was the same; to discover potential metal-poor candidate stars in the halo of the Milky Way, with an emphasis on extremely metal-poor (EMP:  $[\text{Fe}/\text{H}] < -3.0$ ) and ultra metal-poor (UMP:  $[\text{Fe}/\text{H}] < -4.0$ ) stars.

Using the same catalogue of sources as Jenkins et al. (2019), I was able to initially adopt and improve their approach to identify 165 metal-poor candidates.

I used 102 theoretical spectra from the POLLUX database with complete integer metallicities ( $[\text{Fe}/\text{H}]$ ) of 0 to -5 to compute magnitude values for multiple filters: *NB392*, *g*, *u* and *i*, which were then used to estimate metallicities of the 165 candidate metal-poor stars via colour-colour plots and metallicity heatmaps.

16 EMP and 38 UMP candidate stars were identified. The correlation between temperature and *g-i* values was also explored and used to classify the 165 candidates. The distance of the stars with a  $[\text{Fe}/\text{H}] < -3$  was estimated based on approximations and I found that 41 UMP and EMP candidates sit within 66kpc, and therefore can be reasonably approximated to sit within the Milky Way Halo.

Number densities for the candidate F,G and K-type stars identified in this study are  $(1.50 \pm 0.81) \times 10^{-13} \text{ pc}^{-3}$ ,  $(7.64 \pm 1.89) \times 10^{-12} \text{ pc}^{-3}$  and  $(1.91 \pm 0.34) \times 10^{-9} \text{ pc}^{-3}$  respectively, which follows the pattern reported in literature. Finally, I created a metallicity distribution function (MDF) for the candidate stars which follows the predicted MDF and F-type stars are shown to peak around  $[\text{Fe}/\text{H}] = -1.5$  which is close to the literature value of  $[\text{Fe}/\text{H}] = -1.6$ .

# 1

## Introduction

Research into metal-poor stars (where a metal is defined as any element heavier than helium Prochaska et al. 2003) has become more prevalent as they can provide valuable insights in astronomy. Namely supernovae and the physics of these early explosions. Number densities and metallicity distributions (both of which will be examined in their own sections) can also be explored using these ancient stars (Starkenburg et al., 2017).

The idea that metal-poor stars can be used to explore and infer the conditions of the early Universe, just a few billion years after the Big Bang, is one that has slowly formed over decades.

In lieu of accurate methods for directly calculating the age of most old stars, the age is determined via its chemical abundance profile. It is widely assumed that the more metal-poor a star, the older it is (Frebel & Norris, 2015).

### 1.1 Characteristics of Stars

The most basic characteristics of a star are its metallicity, luminosity, surface temperature and mass (Andersen, 1991). The following sections will go through each topic and make apparent how they are all linked, section 1.2 will explain how we can use these basic quantities to classify stars.

### 1.1.1 Metallicity

Metallicity of a star can be determined by calculating the abundance of an element with respect to another, a logarithmic ratio of the two is used in comparison to the Sun. The notation is usually defined like this:

$$[A/B] = \log_{10} \left( \frac{N_A}{N_B} \right)_* - \log_{10} \left( \frac{N_A}{N_B} \right)_{\odot} \quad (1.1)$$

where  $N_A$  and  $N_B$  are the number of atoms of the elements A and B, with  $*$  and  $\odot$  referring to the star in question and the Sun respectively. There are a significant number of absorption lines from the Sun that can be attributed to Fe atom transitions. Therefore, Fe is the traditional reference element used for comparisons of metallicity between two stars (Beers & Christlieb, 2005). Because it is a logarithmic scale in relation to the Sun, a star with a metallicity of  $[\text{Fe}/\text{H}] = -1$  indicates the object would have 1/10th of the metallicity of the Sun (Norris et al., 1993).

#### 1.1.1.1 Nomenclature

Beers & Christlieb (2005) proposed a standard notation for categorising metal-poor stars. The standard nomenclature is tabulated below and will be used throughout this thesis.

[Fe/H]	Term	Acronym
>+0.5	Super metal-rich	SMR
0.0	Solar	-
<-1.0	Metal-poor	MP
<-2.0	Very metal-poor	VMP
<-3.0	Extremely metal-poor	EMP
<-4.0	Ultra metal-poor	UMP
<-5.0	Hyper metal-poor	HMP
<-6.0	Mega metal-poor	MMP

**Table 1.1:** Nomenclature of stars for different metallicities.

### 1.1.2 Luminosity, Flux and Magnitudes

The luminosity of a star is the total amount of energy transmitted by the object per second and is usually assumed to be emitted equally in all directions. It is intrinsically linked to flux ( $f$ ) and distance of a star via the inverse square law, this highlights that luminosity cannot be observed or measured directly and so has to be indirectly explored through the flux:

$$f = \frac{L}{4\pi d^2} \quad (1.2)$$

as the distance increases the luminosity decreases and the luminosity is dependent on a parameter termed the luminosity distance ( $d$ ).

Magnitude is directly related to luminosity and flux and is a way of assessing brightness. Apparent magnitude is the brightness of the star as we see it from earth. When the star is theoretically placed 10pc from the observer, this is called the absolute magnitude. (Zeilik & Gregory, 1998).

### 1.1.3 Filters and Magnitude Systems

Electromagnetic radiation detectors are sensitive only over given wavelength bands. Our eyes for example can only take in visible light and are most sensitive to green and yellow and so the visual magnitude ( $m_v$ ) is associated to wavelengths surrounding 540nm. As an unlikely example, if a star only radiated light in the infrared region, it would be invisible to the naked eye regardless of the amount of radiation produced (Zeilik & Gregory, 1998). Fortunately, real starlight usually encompasses a whole range of wavelengths and colours. Out of blue, orange and yellow stars, the latter will appear brighter to us, due to our eyes being green-yellow sensitive.

A photographic plate was the first way magnitudes were quantitatively measured, however these plates were sensitive primarily to blue light, and photographic magnitude ( $m_{ptg}$ ) is still centred around this colour at 420nm. This led to the devising of magnitude systems by using filters in conjunction with photoelectric photometers to measure magnitudes in the infrared and ultraviolet.

A photoelectric magnitude system is made up of a detector, filters and a calibration in energy units. A filter has two important properties, the full width at half maximum (FWHM) also known as the bandpass ( $\Delta\lambda$ ) and the effective wavelength ( $\lambda_0$ ), which coincides with the peak transmission wavelength.

There are three main filter types:

1. broadband -  $\Delta\lambda \approx 100$  nm
2. intermediate -  $\Delta\lambda \approx 10$  nm
3. narrow-band -  $\Delta\lambda \approx 1$  nm.

A trade off must be made when choosing a filter based on  $\Delta\lambda$  between the amount of flux being detected and the spectral information. More narrow band filters give more spectral information, however there are longer integration times of flux due to the decrease in admission.

Figure 1.1 shows the transmission profiles of the filters used in this study: *NB392*, *u*, *g* and *i*.

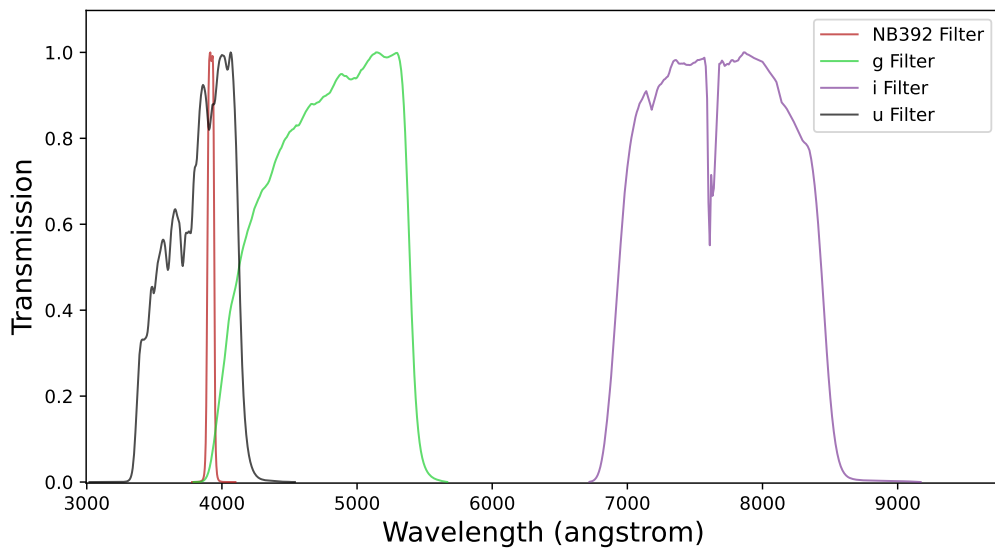


**Figure 1.1:** The transmission profiles of the filters used in this study *NB392*, *u*, *g*, and *i*.

The *UBV* system is a commonly used broadband magnitude system, it is a combination of ultraviolet (*u*) blue (*B*) and visual (*V*) magnitudes. Due to the

development of CCDs the *UBV* system has been extended to the red and infrared with *R* and *i* in the far red and *J*, *H*, *K*, *L* and *M* in the infrared.

### 1.1.4 Temperature and Blackbody Radiation

A colour in astronomy is defined as the difference between two magnitudes for the same source from different filters and is really a flux ratio illustrated by:

$$m_2 - m_1 = -2.5 \log_{10} \frac{f_1}{f_2}. \quad (1.3)$$

where  $m$  and  $f$  are the magnitude and flux values. There is a direct relationship between the temperature of a star and its colour, a “cooler” star is more red and a hotter star is more blue and so colour provides an easy way of identifying a star’s temperature (Kaler, 2011).

Although stars are not perfect blackbodies the aforementioned relationship can be explained by treating them as such. A perfect blackbody is an object that absorbs all of the incident electromagnetic radiation without reflection, and then re-emits the radiation in line with a blackbody spectrum, the shape of which is determined by temperature.

The shape of the curve is described by a mathematical function called the Planck function which describes the continuum of radiation released by all stars in thermal equilibrium.

Figure 1.2 shows that as the wavelength of the light gets longer, there is a gradual rise in radiation intensity up until a peak ( $\lambda_{max}$ ). The wavelength of  $\lambda_{max}$  is inversely proportional to the temperature ( $T$ ) of the blackbody. This phenomenon is described by Wien’s Law with:

$$\lambda_{max}T = 2.898 \times 10^{-3} \text{mK}. \quad (1.4)$$

Different wavelengths correspond to different colours, therefore according to Wien’s Law, a hotter object will have a different colour to a cooler object (Kardaras & Kallery, 2020).

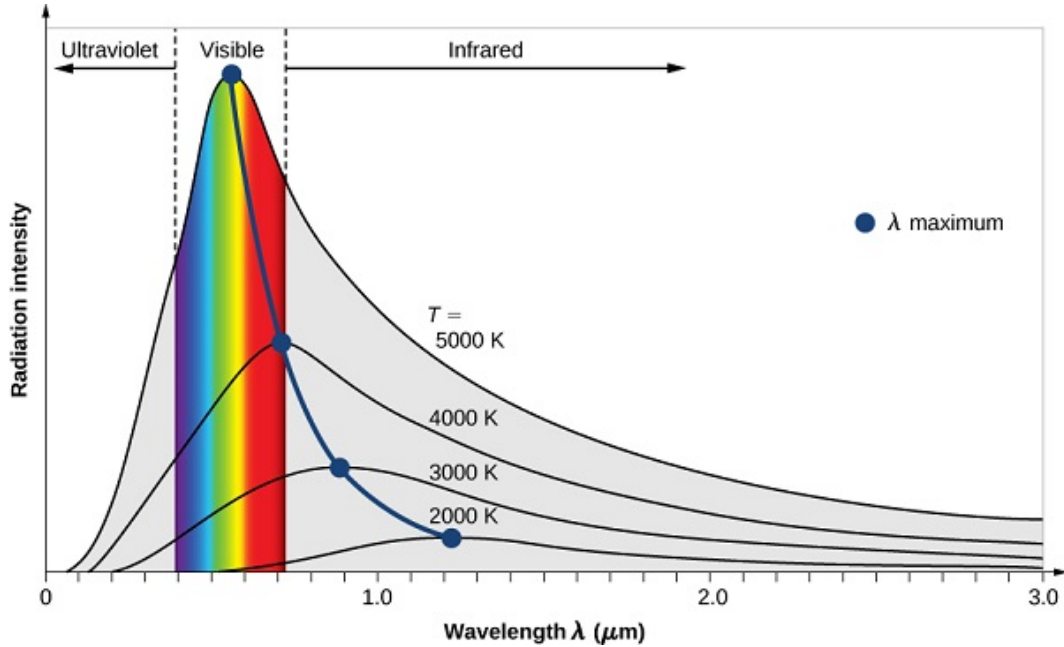


**Figure 1.2:** Diagram representing how blackbody radiation changes with temperature taken from Libretexts (2022)

The intensity of the radiation emitted can be described by the Stefan-Boltzmann Law, which states that the intensity is related to temperature raised to the fourth power and its. This law also relates temperature and luminosity together:

$$L = 4\pi R^2 \sigma T_{eff}^4 \quad (1.5)$$

When the temperature of a star is found like this *i.e.* by approximating it as a blackbody, it is termed the effective temperature ( $T_{eff}$ ) Eker et al. (2021).  $R$  is the radius of the star and  $\sigma$  is the Stefan-Boltzmann constant.

### 1.1.5 Mass

As has been discussed, the temperature of a star determines the colour and the luminosity determines brightness. Both of these are almost exclusively dependent on the star's mass. The mass of a star is reported in relation to the solar mass ( $M_{\odot}$ ).

Furthermore, the mass of a star is related to its stellar lifetime, the larger the object is the more luminous and hotter it is, and so the star burns through its fuel quicker.

The exact mass of a stellar object can be difficult to measure and so the mass-luminosity relationship (MLR) is important for estimating this physical quantity. This relation states that luminosity and mass are linked through the following power-law:

$$\left(\frac{L}{L_{\odot}}\right) = \left(\frac{M}{M_{\odot}}\right)^a \quad (1.6)$$

For low-mass stars on the main sequence (section 1.2.2),  $a$  is approximately equal to 4. The MLR can also help construct the Initial Mass Function from the luminosity function of stars (Wang & Zhong, 2018).

## 1.2 Using Stellar Characteristics to Classify Stars

The following sections will bring all the properties of stars together and show how they can be used to investigate and classify stars.

### 1.2.1 Spectroscopy

#### 1.2.1.1 Balmer Lines Leading to OBAFGKM

Historically, the common absorption features of hydrogen (Balmer lines) in stellar spectra were used to divide stars into spectral classes, this was the first quantitative step in classifying stars. The most prominent astronomers that worked on this were Williamina Fleming, Antonia Maury and Annie Jump Cannon. The stars were classified alphabetically with those objects that displayed the strongest (deepest) Balmer lines at the start (A) and stars with weaker Balmer lines towards the end of the alphabet (Giridhar, 2010).

However, Maury, Cannon and Edward Charles Pickering reordered the initial system to a non-alphabetic one which reflected the surface temperatures of the classes. The current spectral sequence is: OBAFGKM, which can be remembered

using the mnemonic Oh Boy! Another Freaking Giraffe Kicked Mum. This ranking is presented in a highest to lowest fashion in terms of luminosity, temperature, size and mass.

A letter class can be further divided using a numeric digit with 0 being the hottest and 9 being the coolest *e.g.* A8, A9 F0 and F1 display a sequence of stars going from hottest to coolest. Sub-classes are then defined which link to surface temperature (Giridhar, 2010).

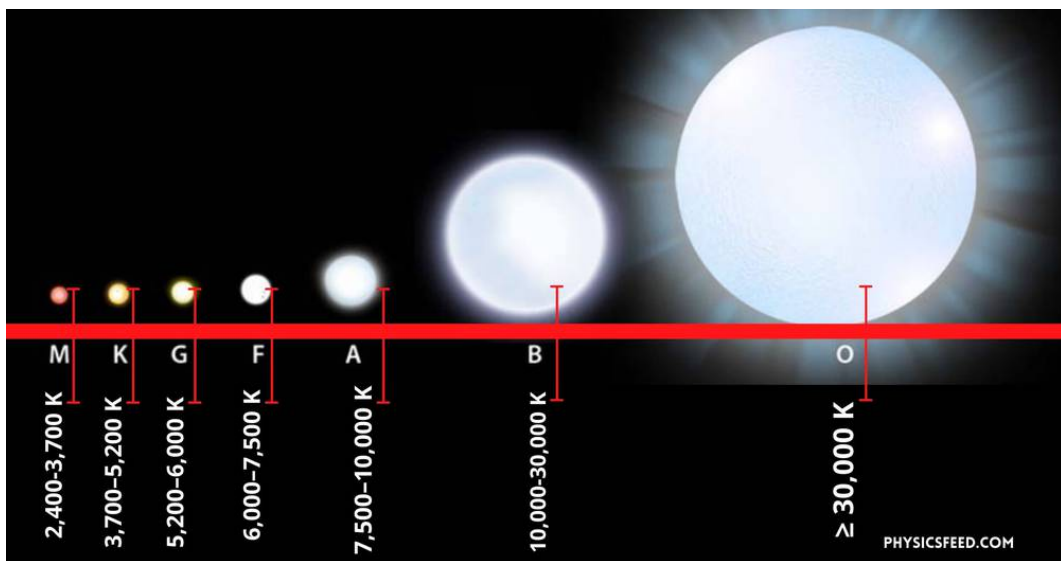


**Figure 1.3:** A diagram showing the different spectral classes with their specific temperatures (Gotame, 2020).

O stars are the biggest, brightest and hottest stars with a blue colour, M stars are the coolest, smallest and dimmest stars with a more red colour.

### 1.2.1.2 CaHK Absorption Lines

The spectra of extremely low metallicity stars are vacant of metal lines and so the abundance of only a few elements can be analysed (Osorio et al., 2022).

In section 1.1.1 it is noted that Fe is a traditional reference element for metallicity. For the most metal-poor stars that have shallow absorption lines - where these are hard to differentiate from the signal to noise ratio - the Fe content can be difficult to measure.

The Fraunhofer CaHK absorption lines occur at  $3969.59\text{\AA}$  and  $3934.78\text{\AA}$  (Zhu & Ménard, 2013). They highlight the calcium abundance and are much more prominent lines in stellar spectra. Frebel (2010) reported that these are still the best lines to indicate the overall metallicity of a metal-poor star. This is because Ca and Fe are generated via similar fusion processes. Therefore, the CaHK absorption lines can be used as a good candidate for calculating metallicity in metal-poor stars as they are a good indication of  $[\text{Fe}/\text{H}]$  (Beers et al., 1990).

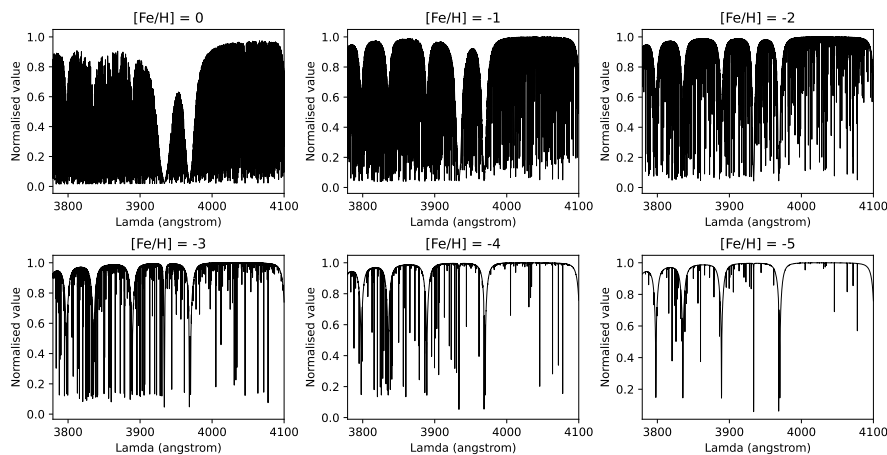


**Figure 1.4:** A demonstration of how the CaHK absorption can vary in relation to metallicity for a G-type star sourced from the Pollux database.

Figure 1.4 demonstrates that as metallicity decreases the absorption of the CaHK lines diminishes as a result of there being less Fe and Ca.

### 1.2.2 Hertzsprung-Russell Diagrams

A Hertzsprung-Russell (HR) diagram is shown in figure 1.5. These plots are of the luminosity/brightness of stars against their surface temperatures (or the spectral type against absolute magnitude) and are one of the most popular tools used by astronomers to gain knowledge about a star's age, size, temperature, luminosity and eventual death. They also give information about how the different spectral classes fit together and stellar evolution (Airey & Eriksson, 2019).

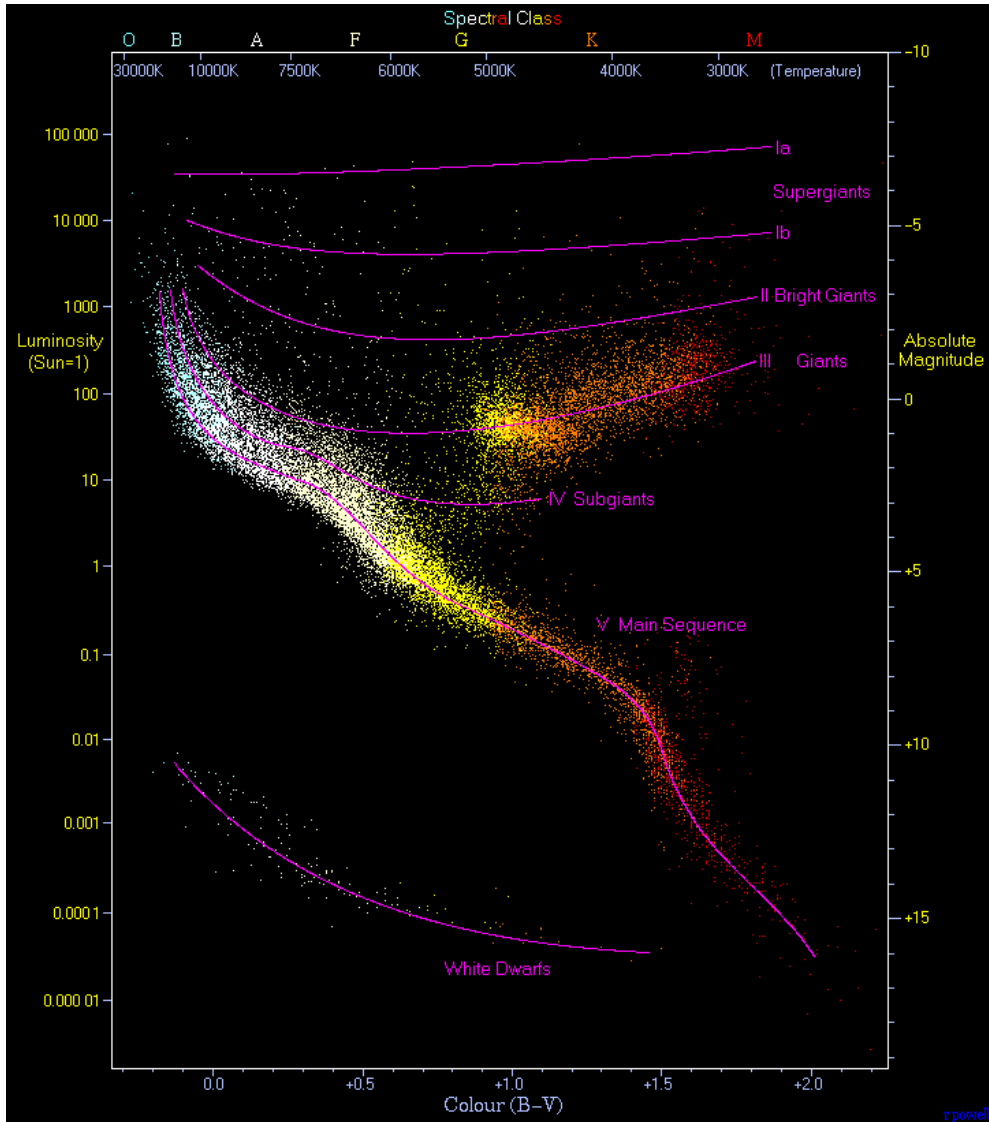


**Figure 1.5:** A Hertzsprung-Russell Diagram taken from Universe today showing the different regions such as the main sequence and red giants (Johnston, 2022).

Initial mass of a star determines what evolutionary stages it goes through and stars at different stages of their evolutionary cycle occupy different regions of the HR diagram.

There are 4 main regions that represent evolutionary stages:

1. Main Sequence - this is the most prominent feature and spans the whole diagram with hot, luminous stars lying on the upper left of the region and cooler, fainter stars lying on the bottom right *i.e.* the mass-luminosity relationship is followed. This period is where a star spends the majority of its life. Time is spent burning hydrogen into helium in the stellar cores.
2. Red Giants and Super Giants - When the hydrogen in the core has been fully depleted, the equilibrium governing the star fails and gravity wins, leading to the star collapsing. Due to the extreme pressures and temperatures the conditions are perfect for the fusion of helium into heavier elements such as carbon, oxygen and nitrogen. The outer layers of the star expands and smaller mass stars turn into red giants and bigger mass stars evolve into supergiants. Both of these stages are short on astronomical time scales.
3. White Dwarfs - This is the final evolution stage of stars a similar size to the Sun and occurs after most of the outer material has been expelled. A hot, dense core, made mostly of carbon, nitrogen and oxygen is all that remains. Despite being extremely hot, white dwarfs originating from solar mass stars have low luminosities due to their small size. As shown in 1.5 white dwarfs can have a wide range of temperatures. The star stays in this stage for billions of years whilst it slowly cools down.

Stars that are significantly more massive than the Sun have different fates and eventually turn into neutron stars and blackholes. Both of these phenomena cannot be seen in the HR diagram.

## 1.3 Stellar Formation and Populations of Stars

### 1.3.1 Star Formation

In a giant molecular cloud (GMC) turbulent motions lead to overdense regions. Stars and star clusters are formed after these regions reach the “Jeans critical mass” where gravity dominates and as a consequence initial collapse of the region occurs under free fall. Overdensities tend to form towards the centre, these regions tend to reach and exceed the Jeans critical mass sooner leading them to collapse faster, this is termed as inside out collapse.

The gas in the GMC at this initial collapse stage is optically thin because radiation is free to escape and the cloud is also said to be isothermal. The density is still increasing rapidly, and so the Jeans mass is decreasing and fragmentation occurs.

Contemporary star formation also requires a component of cooling of the gas to lead to fragmentation. Metal-line cooling (where energy is radiated away from the system due to excited metal atom collisions) and dust cooling (where dust absorbs and reradiates some energy of the gas) are the two main ways in which this occurs (Klessen et al., 2012).

Fragmentation is where the original collapsing region forms smaller clumps which can have local density fluctuations leading to collapses of those smaller regions. Areas with higher dust quantities will be more dense, this leads to collapse and fragmentation occurring faster.

As the collapse continues the density continues to increase and so does the Jeans mass with the relationship between these two parameters changing. When the gas becomes optically thick and adiabatic, the smallest fragment reaches a minimum mass and fragmentation stops and the first protostar(s) of the gas cloud is/are formed.

Gravitational contraction leads to the rising of the internal temperature of the protostars created until a threshold is reached which can trigger nuclear reactions in the core. This production of energy causes an outward pressure counteracting the gravitational collapse, eventually an equilibrium is reached in the star which lasts as long as there is the appropriate nuclear fuel in the core (Caputo, 1998).

### 1.3.2 First Stars

Primordial gas clouds contained no metals or dust, therefore, contemporary methods of cooling mentioned in the previous section were not possible. Cooling was instead facilitated by trace amounts of  $\text{H}_2$  present in the parent clouds. This is not efficient and so fragmentation was not possible for the first generations of stars as the Jeans mass would still be high (Caputo, 1998).

These stars are called Population III (Pop III) stars and are thought to have formed in dark matter “minihaloes”, which existed before the formation of galaxies, with masses of  $\approx 10^6 M_\odot$ . These structures were the first to be made of enough  $\text{H}_2$  so that collapse was able to continue. This was through the energy release of rotational and vibrational line emission that cooled the gas that fell into the dark matter minihalo (Clark et al., 2011).

It is generally accepted that the lack of fragmentation due to the inefficiency of the coolant resulted in very massive Pop III stars with a top heavy Initial Mass Function (IMF). Further discussion into the IMF is in section 1.4. Bromm et al. (2002), simulated the formation of Pop III stars and found that the first stars possibly had a mass of  $100M_\odot$  and over. This work is corroborated by Abel et al. (2002), and provides a reason as to why Pop III stars remain so elusive, especially higher mass ones: the more massive a star the shorter its lifetime and so stars with  $100M_\odot$  and higher will no longer be alive for us to witness.

In contrast to this, Stacy et al. (2016), simulated that low-mass Pop III stars could have been formed and are the only possible survivors of these ancient stars.

### 1.3.3 What Spectral Type Will the Low-Mass Pop III Survivors be?

It is possible to estimate what spectral type the low-mass Pop III survivors will be by using the principles of the HR diagram explained in section 1.2.2. The first Pop III stars to evolve off the main sequence will be O-type stars. As mentioned in section 1.1.5 this is because the bigger a star is, the shorter its lifetime as it burns through its fuel quicker. B and A spectral types are the next biggest and hottest and so again will have already burned all of their fuel and branched off

the main sequence. The lower mass stars will still be on the main sequence today, therefore these Pop III survivors are predicted to have spectral types F,G or K. The lowest predictions of the IMF ( $>0.8M_{\odot}$ ) suggest that M-type star formation was very unlikely as they are too small (Komiya et al., 2016).

### 1.3.4 Formation of Population I and II Stars

At the end of a Pop III star's life cycle, one of two things happened, the exploded objects either collapsed into black holes or died as energetic pair-instability supernovae (PISNe). These supernovae polluted the pristine gas with the first metals and dust. As discussed in section 1.3.1 these are now favourable conditions for metal and dust cooling of the pre-stellar clouds which leads to fragmentation occurring when the second generation Population II (Pop II) stars were being formed. This metal and dust enrichment of the primordial gas thereby allows the formation of lower-mass Pop II stars (Frebel, 2010) (Schneider et al., 2006).

Stellar evolution and the eventual deaths of Pop II stars further enriched galaxies with heavier metals and the stars formed from these metal-rich regions are called Population I (Pop I) stars.

### 1.3.5 Properties of Population I and II Stars

In 1944, Walter Baade was credited for classifying stars into the two stellar populations mentioned in the previous section. There are significant differences between the two, especially spectroscopically. Pop II stars are metal-poor and as pointed out in section 1.2.1.2 their spectra are vacant of most metal lines or the absorption lines relating to metallicity and chemical abundances are very shallow. Pop I stars (such as our Sun) are more metal rich and so have higher chemical abundances in their spectra.

The visible part of the spectrum of the Sun is shown in figure 1.6. There are many dark absorption lines called Fraunhofer absorption lines that correlate to the absorption of different elements in the solar atmosphere (Shapiro et al., 2015). Section 1.2.1.2 explained how the H and K Fraunhofer lines can be used

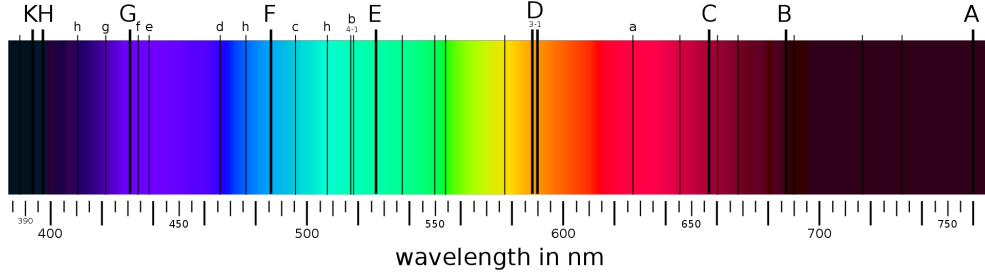


**Figure 1.6:** Visible part of the solar spectrum with the Fraunhofer absorption lines indicated (Commons, 2022).

to classify metal-poor stars, thereby showing that the spectroscopic differences map to physical differences such as metallicity (Gamow, 1948) (Caputo, 1998).

Baade was able to distinct between the two groups using this information and other physical and location differences such as identifying that:

1. Pop I stars are found in the disks of spiral galaxies. They are very luminous, hotter and younger,
2. In contrast to this, Pop II stars are less luminous, cooler and older. They tend to be found in globular clusters and in the halo of galaxies.

## 1.4 The Initial Mass Function

A luminosity function gives the number density of stars as a function of absolute magnitude (Salpeter, 1955). Luminosity functions separated by spectral type can be used to calculate the Initial Mass Function (IMF) which describes the number of stars per stellar mass when stars are born.

As briefly mentioned in section 1.3.2 (Bromm et al., 2002) theorised that the Pop III IMF was top heavy with the characteristic mass exceeding  $\approx 100M_{\odot}$ . This work is backed by (Abel et al., 2002) and (Yoshida et al., 2008) and observational support for this is in fact the lack of an observed Pop III star.

Pop III stars have thus far remained elusive and so the best way to find information about the masses of these stars is through analysing the atmospheric abundances of metal-poor stars. Because the pathways of nucleosynthesis are

extremely sensitive to stellar masses, the relative abundances of elements in the surviving metal-poor stars reflect the masses of Pop III stars (Frebel et al., 2005).

In the last decade or so, high-resolution simulations have predicted that lower-mass stars can form and the mass ranges are between subsolar and thousands of solar masses. These new simulations take detailed physical processes into account, and predict fragmentation of the central gas occurs, hence the various mass ranges projected (Clark et al., 2008) (Stacy & Bromm, 2014).

In 2018, (Ishigaki et al., 2018), used the elemental abundance patterns in EMP stars to infer the IMF of the first stars. They found that stars with an initial mass of  $M < 40$  solar masses best fit the observed abundance patterns of the EMP stars. Over 50% of stars were best fitted by having the initial mass at  $25 M_{\odot}$ . (Latif et al., 2022) showed via 3 body interactions that up to 70% of stars are ejected from their protostellar disks which can limit the final masses of the Pop III stars. Most of these ejected stars were smaller than  $10 M_{\odot}$ .

Despite these findings, the prediction of the IMF remains top-heavy due to the fragmentation still being less efficient and the rates of accretion being significantly higher than present day star formation (Clark et al., 2008) (Stacy & Bromm, 2014).

This is in contradiction to the bottom-heavy IMF that has been observed for the Milky Way by (Chabrier, 2003) where they found the galactic mass function to be below  $1 M_{\odot}$ .

### 1.4.1 Metallicity Distribution Function

The metallicity distribution function is an important concept and tool in stellar and chemical evolution. It can be displayed as a curve and states what proportion of stars have a specific metallicity in a population of stars such as in a cluster or galaxy (Fenner & Gibson, 2003).

The metallicity distribution function (MDF) of halo stars peaks at  $[\text{Fe}/\text{H}] = -1.6$  (Beers & Christlieb, 2005).

This can help yield information about the age and formation of stellar systems. G-dwarfs in the solar neighbourhood have been thoroughly researched due to the fact that these type stars can help the most in constraining the chemical evolution

in the early galaxy. This is because although they are bright enough to be studied they are still relatively unevolved.

Understanding the chemical evolution of the galaxy leads astronomers to clues about the formation history of the Milky Way, such as whether the Milky Way formed from a single primordial gas cloud.

However, when trying to constrain the MDF and study galactic chemical evolution there is something called the G-dwarf problem. This relates to the fact that in reality there are not enough metal-poor G-type stars observed compared to what is predicted by simple chemical evolution models (Greener et al., 2021). As a result of this many predictions of the MDF show a metal-poor tail (Prantzos, 2008) (Christlieb et al., 2004).

In 2001, (Bekki & Chiba, 2001) pioneered an attempt to account for the observed metallicity distribution in the halo of the Milky Way. After modelling an analogous galaxy to the Milky Way and despite the spatial resolution of the simulations to be low (2 kpc), they were able to produce a metallicity distribution with a peak at the observed metallicity: ( $[\text{Fe}/\text{H}] = -1.6$ ). However, the shape is a lot narrower than the observed one. Another discrepancy was the double peak in the distribution, this is not observed in the actual metallicity distribution of the halo. This can be attributed to the low-mass resolution (Prantzos, 2008). More recently, An et al. (2015) found that the inner and outer halos peak at  $[\text{Fe}/\text{H}] \approx -1.4$  and  $-1.9$  respectively.

## 1.5 Metal-Poor Stars

There were discrepancies between stellar classifications of stars based on whether Balmer lines of hydrogen were used or other characteristics such as the strength of metallic lines. Chamberlain & Aller (1951) were the first to quantitatively analyse the spectra of two stars thought to be A-type subdwarfs. By realising the stars were more metal-deficient than the Sun they were able to understand the differences and reclassify the stars as metal-poor F-type stars.

The research into metal-poor stars was dominated by US astronomers until around 1964 where French astronomers (Cayrel de Strobel, 1966) presented

spectrophotometric work on three metal-poor stars (Cayrel de Strobel, 1966). Bond (1970) used objective prism plates with the purpose of initiating the first systematic search for metal-poor stars.

The next big milestone in metal-poor star discovery came in 1985 with (Beers et al., 1985), reporting results from another objective-prism survey for low metallicity candidates. They present a list of 134 VMP stars, and 1993 in which (Norris et al., 1993) analysed high resolution spectra and the chemical abundances of 4 metal-poor stars that were presented in the aforementioned survey.

The stars discovered over the last few decades have been getting decreasingly metal-poor. (Keller et al., 2014), discovered SMSS J0313-6708 and with a  $[\text{Fe}/\text{H}] < -7.3$ , it is currently the most metal-poor star known.

### 1.5.1 Techniques to search for metal-poor stars

Decades worth of research has shown that metal-poor stars are very rare and so trying to obtain chemical abundances for them has proven difficult and long. Out of 100,000 field stars it is expected that only one would have a metallicity equal to or below  $[\text{Fe}/\text{H}] = -3$  (Frebel & Norris, 2015). The whole process can be split into three major observational steps (Beers & Christlieb, 2005):

1. A wide angle survey is carried out and candidate metal-poor stars are selected,
2. To confirm the identity of candidates that are actually metal-poor, moderate-resolution spectroscopy is used,
3. The most interesting candidates are followed up with high-resolution spectroscopy.

The next few sections will give a brief overview on the different ways of how step 1 can be carried out.

### 1.5.1.1 Proper-Motion-Based Searches

Proper-motion is using the values of precise stellar positions to measure the angular velocities of stars across the sky. Stellar objects in the halo generally have higher proper-motions than those in the galactic disk. (Frebel & Norris, 2015) Astronomers have used this information to probe the galactic halo for stars with high proper-motions. Broadband photometry was used to study these stars which made use of the direct relationship between metal deficiency in the stellar atmospheres and flux. Photometric estimates (where the absorbance of light at specific wavelength allows for the calculation of chemical abundances) then allowed the calculation of metallicity of these objects with high proper-motions (Beers & Christlieb, 2005). Using this technique, Carney & Peterson (1981) discovered the first star with a  $[\text{Fe}/\text{H}] < -3.0$ .

### 1.5.1.2 Objective-Prism Surveys

Objective-prism spectroscopy entails a prism being placed in front of the telescope. The light from a star in the field of view goes into the telescope and passes through this prism, causing the light to disperse and produce a spectrum on a photographic plate (Beers & Christlieb, 2005).

Objective-prism surveys allow for the production of low-resolution spectroscopy of many stars simultaneously (Frebel & Norris, 2015). In section 1.5 I pointed out that Bond (1970) carried out the first major objective-prism survey to identify metal-poor stars.

The HK objective prism survey of Beers et al. (1985) used CaHK lines to identify 134 VMP stars. Another notable effort is the Hamburg/ESO survey (HES: (Wisotzki et al., 1996)) which was originally intended to find bright quasars. However, Christlieb et al. (2008) again used the strength of CaHK lines and  $B - V$  colours of objects in the HES to select candidate metal-poor stars.

### 1.5.1.3 Spectroscopic Surveys

The Sloan Digital Sky Survey (SDSS) (York et al., 2000) is a large scale spectroscopic survey that has produced deep-multicolour images that span more than

a quarter of the sky. SDSS-II contained the Sloan Extension for Galactic Understanding and Exploration (SEGUE) which is an imaging and spectroscopic survey of the Milky Way (Yanny et al., 2009).

Starkenburger et al. (2017) present the Pristine survey in which they use narrow-band photometry in the northern hemisphere to focus on CaHK lines in order to search for metal-poor stars. Pairing the CaHK filter with SDSS/SEGUE broadband  $g$  and  $i$  photometry (Starkenburger et al., 2017) show this method is a powerful tool for selecting metal-poor stars by deriving photometric metallicities with uncertainties of only  $\approx 0.2$  dex.

#### 1.5.1.4 Photometric Surveys

Photometry measures the amount of flux or the intensity of the light radiated by astronomical objects and provides another low-resolution method for the discovery of metal-poor stars.

The Southern Sky Survey conducted by the survey telescope SkyMapper used filters specifically made for the optimal determination of characteristics pertaining to metal-poor stars such as temperature and metallicity. They were a modification of the filter set used by SDSS. This survey led to the discovery of SMSS J0313-6708 (Keller et al., 2014).

## 1.6 Motivations and COSMOS

The aim of this thesis is to essentially attempt the first major observational step as described in section 1.5.1.

The Cosmic Evolution Survey (COSMOS) is a project undertaken by the Hubble Space Telescope (HST) to image a two square degree field of sky commonly known as the COSMOS field. Its primary purpose was to be used in the research of galaxy formation and evolution and this patch of sky was chosen as it corresponds to a region that has a relatively unobstructed view of the galactic halo and is easily accessible for observatories to study in the northern and southern hemisphere (Scoville et al., 2007).

Jenkins et al. (2019) carried out an investigation (hereby referred to as WARP) in which the aim was to use the COSMOS field to survey a portion of the Milky Way halo in the attempts to find Pop III stars or their direct descendants, *i.e.* Pop II metal-poor stars. Covering 1.89 deg<sup>2</sup>, and going 5-7 magnitudes deeper than the Pristine survey, WARP discovered 7 stars with a [Fe/H] of -3 or below. They also investigated number densities and metallicity distributions of metal-poor stars in the galactic halo.

The purpose of this study is to initially adopt the approach of (Jenkins et al., 2019), with improvements, to identify a cleaner and larger sample of EMP and UMP stars in the same dataset.

## 2

# Catalogue and Data

The 2.54m Isaac Newton Telescope (INT) is currently situated at the Roque de los Muchachose observatory in the canary islands and has been there after being moved from the Royal Greenwich Observatory in 1979. The telescope is usually used with the wide field camera (WFC), which consists of 4 CCDs and has a field of view of  $0.56 \times 0.56$  sq degrees or 0.33 arcminutes.

Sobral et al. (2017) carried out the CALYMHA survey, which is a survey of the COSMOS field using Lyman  $\alpha$  lines to select high redshift galaxies. Using the INT/WFC from 2013 to 2015, (Sobral et al., 2017) used a narrowband filter - *NB392* ( $\lambda_c = 3918\text{\AA}$ ,  $\Delta\lambda = 52\text{\AA}$ ) and several broadband filters to take a survey in order to observe distant galaxies.

The deepest images reached a  $M_{NB392} = 25$  and the area of sky surveyed was  $1.43 \text{ deg}^2$ .

In section 1.2.1.2 above I described how the CaHK lines can be used as a proxy for overall metallicity in a stellar atmosphere reported as  $[\text{Fe}/\text{H}]$ .

The filter profiles used in this study are shown in figure 1.1. The *NB392* filter covers the part of the spectrum that contains the characteristic CaHK absorption lines. There is a good separation of the peaks for the filters *g* and *i*. This can be used for the y axis to create colour-colour plots eventually leading to the estimation of magnitudes, metallicities, spectral types and number densities.

The y-axis of the colour-colour plots and heatmaps in this study use  $NB392 - g - (g - i)$ , WARP chose to use  $NB392 - u - (g - i)$ , however, as will be explained

---

in section 5.3  $NB392 - g - (g - i)$ , gave a better separation of theoretical stars at lower metallicities.

From Sobral et al. (2017) came a catalogue of 123,505 sources (hereby known as the CALYMHA catalogue).

# 3

## Identifying potential metal-poor candidates

Below I describe the procedures used to cross-match the existing catalogues of the COSMOS field so I could separate stars from galaxies and identify metal-poor stellar candidates. I also used COSMOS images provided by ACS to perform a visual inspection as the locations of the sources are covered by the COSMOS field. This is for completeness but also because Sobral et al. (2017) created this data-set to study high redshift galaxies many of the sources will be galaxies.

### 3.1 Catalogue Matching

I used TOPCAT (Miller, 2007) to cross match the COSMOS and CALYMHA catalogues accepting the closest match between  $3''$ , this accounts for any stars in the halo with high proper-motions having moved since the data was taken from 2013-2015 and any astrometric offsets. This resulted in a catalogue of 94,591 matches, hereby known as the RUBY catalogue.

## 3.2 Limiting Magnitude

The limiting magnitude is the faintest magnitude that can be reliably detected in the observations. The survey may have a lower probability of detecting fainter objects than the limiting magnitude, but detection of objects fainter than the limiting magnitude will be highly incomplete. I determined the limiting magnitude of the RUBY catalogue empirically.

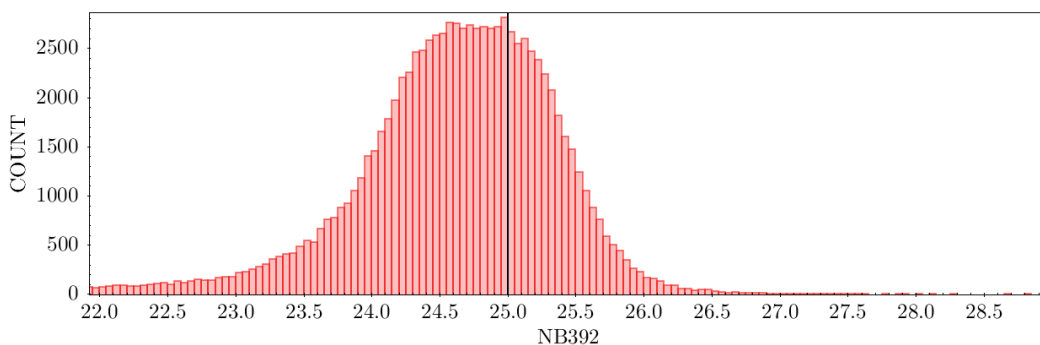


**Figure 3.1:** A histogram of NB392 magnitudes for the RUBY catalogue with a line showing the limiting magnitude to be 25.

By plotting a histogram of the RUBY catalogue using *NB392* magnitudes, the limiting magnitude was determined to be 25 as indicated by the black line in figure 3.1. This value was also chosen as it matches the deepest magnitude reported by (Sobral et al., 2017). Past this point the detections are not clear and so these sources are not included, this value will be in section 3.4.

## 3.3 Star-Galaxy Cut

Stars sit within the galactic halo, this means they have no relative movement to the Milky Way. Galaxies on the other hand move away from the Milky Way. This consequences in stars having a redshift of 0 and galaxies a redshift of non-zero.

I created two subsets (potential stars for cut - PSFC, and potential galaxies for cut - PGFC) in the RUBY catalogue, based on the redshift determinations. In these subsets I only used objects with spectroscopic redshifts from COSMOS,

Step	Description	No. of sources
0	RUBY catalogue	94,591
Pre star-galaxy cut (spectroscopic redshifts)		
1	Using spectroscopic redshifts to create PSFC subset	330 stars
2	Removing extreme sources from PSFC	284
3	Using spectroscopic redshifts to create PGFC subset	3045 galaxies
4	Removing extreme sources from PGFC	2765
Post star-galaxy cut (colours)		No. of potential stars
5	Application of cut (eqn 3.1) to RUBY catalogue using colours	20,309
6	Removing sources with extreme colours	9871
7	Error and magnitude limits applied	2633
8	CLASS_STAR	281
9	Visual inspection	165

**Table 3.1:** Summary of the steps taken to reduce the RUBY catalogue from 94,591 sources to the final 165 potential metal-poor candidates.

because these allowed me to confirm the distinction between the stars and galaxies. These spectroscopic redshifts take a lot of observing time and therefore most COSMOS/RUBY sources do not have these values and are not eligible to be used in determining where to put the cut (*i.e.* in figure 3.2). However, sources without spectroscopic redshifts do have known colours and can be selected once the position of the cut is determined (*i.e.* included in figure 3.3). PSFC should contain only stars as the sources all had a redshift of 0, this gives a total of 330 sources. However, it must be stressed this assumption will only provide an estimate of the number of actual stars as having a redshift of 0 could just mean the redshift could not be measured.

Therefore, this is a first pass cut that can remove unresolved galaxies as long as the COSMOS catalogue was able to estimate a redshift. PGFC contains what are thought to be galaxies as the sources have a redshift of 0.5-7, this gives 3045 galaxies.

Some sources in PSFC have extreme magnitudes, these occurred because some  $U$ ,  $J$  and  $K$  values had values of 99 in the COSMOS/CALYMHA catalogues, which indicates a non-detection in that filter. These sources were removed and PSFC was reduced to 284 sources. A similar method was applied to PGFC where the potential galaxies with extreme magnitudes were removed and so PGFC was

reduced to 2765 sources.

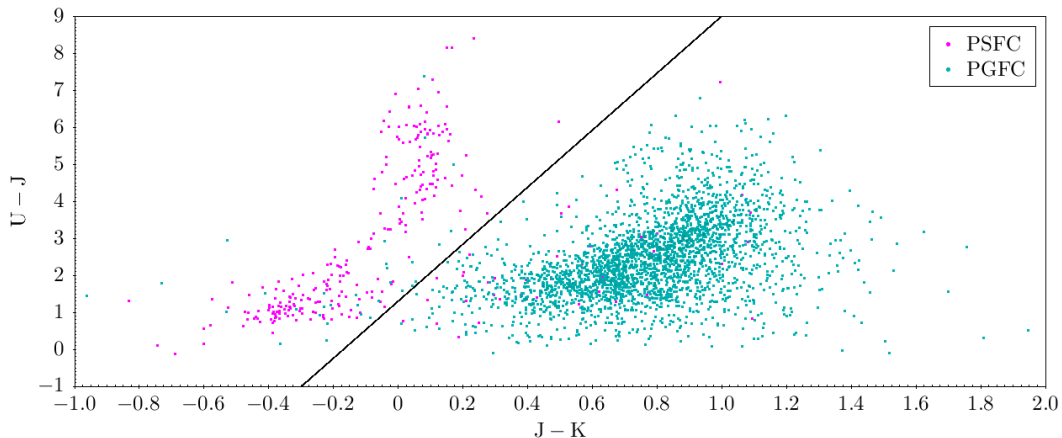


**Figure 3.2:** A sample of potential stars and galaxies separated using the magnitude differences  $U - J$  vs  $J - K$ .

The subsets were plotted and a star-galaxy cut was created by changing the colours of the axis until a separation between stars and galaxies was apparent (*e.g.*  $U - J$  vs  $B - V$ ). The plot that defined the most clear separation between stars and galaxies was  $U - J$  vs  $J - K$ . This makes sense as these colours capture the clear differences between typical stars that peak at shorter wavelengths and galaxies which will peak more into the near infra-red.

The black line in figure 3.2 is a cut placed at this separation and is given by equation 4.1. Sources placed above this line were considered to be stars and anything below this line were considered to be galaxies.

The equation of the cut line is:

$$(U - J) = 7.7(J - K) + 1.3, \quad (3.1)$$

I then calculated an estimate for the completeness and contamination, the method of which is shown in Appendix A.1. The completeness of the PSFC is 85% and the contamination is 12%.

At this stage the completeness and contamination are just estimates, because I am assuming everything in PSFC is a star, it will become apparent as the investigation continues that this is not the case.

Although the extremely red stars under the line in the galaxy area are the sort of stars I would be looking for, placing a cut towards the more red side would mean the contamination would be too high. This line was chosen as the best compromise between completeness and contamination.

The cut was then applied to the whole RUBY catalogue (most of which do not have spectroscopic redshifts) to get 20,309 sources. After removing extreme  $U - J$  and  $J - K$  values by using the condition,

$$(U - J) < 20 \text{ and } -20 < (J - K) < 40 \quad (3.2)$$

this cut down the number of sources to 9871 and they are shown in figure 3.3.

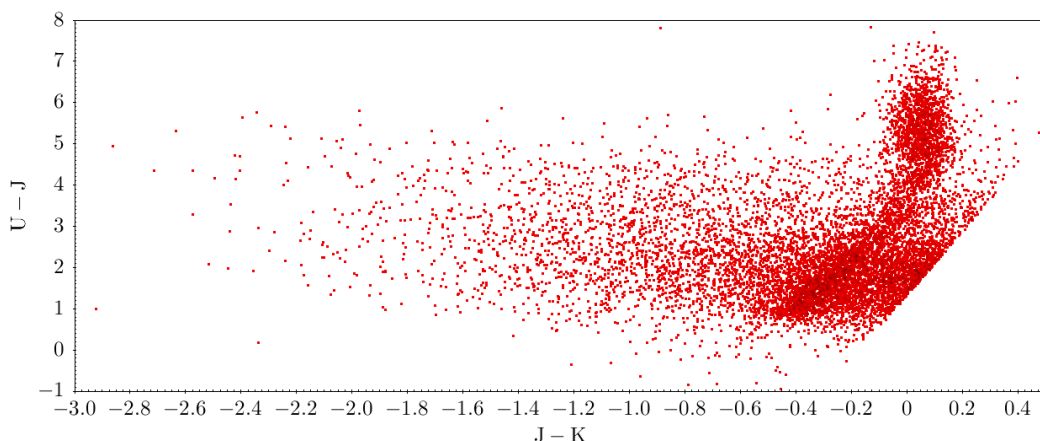


**Figure 3.3:** The catalogue of sources after removing the galaxies identified by a star-galaxy cut.

### 3.4 Errors

As can be seen in later colour-colour plots, the x and y axis were chosen to be  $NB392 - g - (g - i)$  and  $(g - i)$  respectively. By combining the errors for the sources in the  $NB392$ ,  $g$  and  $i$  filters, I calculated the uncertainties for each potential star's x and y value on figure 3.3.

$\sigma_x$  and  $\sigma_y$  were the error in the magnitude differences  $g - i$  and  $NB392 - g - (g - i)$  respectively. These values were calculated using standard error analysis.

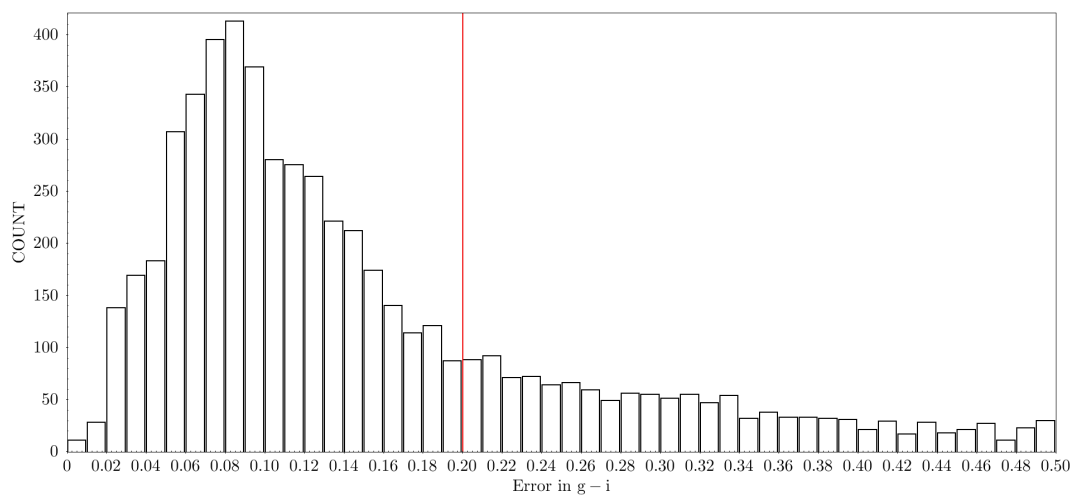


**Figure 3.4:** A histogram of the errors in  $g - i$  ( $\sigma_x$ ) for the 9871 sources with the limiting error indicated to be 0.20.

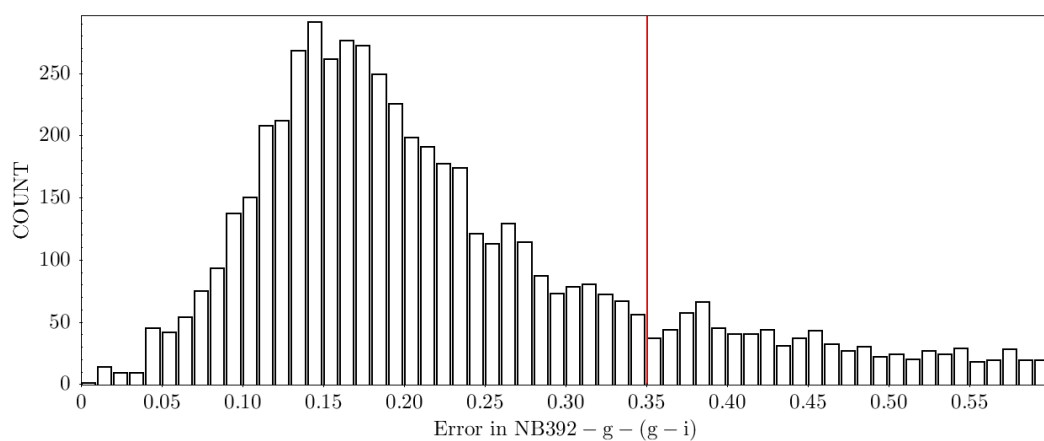


**Figure 3.5:** A histogram of the errors in  $NB392 - g - (g - i)$  ( $\sigma_y$ ) for the 9871 sources with the limiting error indicated to be 0.35.

Histograms were used to find where to limit the errors in  $\sigma_x$  and  $\sigma_y$  to further reduce the number of sources, as shown in figures 3.4 and 3.5. Any sources with an error  $\sigma_x > 0.20$  and  $\sigma_y > 0.35$  were removed. This ensured any extreme errors were removed.

These error limits and the magnitude limit (from section 3.2) were applied to the remaining sources and this resulted in 2633 sources.

### 3.5 CLASS\_STAR

Source Extractor (SExtractor) (Bertin & Arnouts, 1996) is a software that classifies sources from astronomical images and can be used as a reliable star galaxy separation tool. Galactic images commonly tend to be more fuzzy and extended in comparison to stars, which are more point-like. CLASS\_STAR is an internal classifier of SExtractor and outputs the stellarity index. This indicates the probability of how point-like a source is, with a value of 1 meaning there is a high probability the source is a star and 0 meaning it is likely a galaxy. There are some limitations, as quasars have been classified as stars in the past, due to real data differing from training data. However, the classifications of sources with CLASS\_STAR values closer to 0 or 1 are reliable and can be used with confidence.

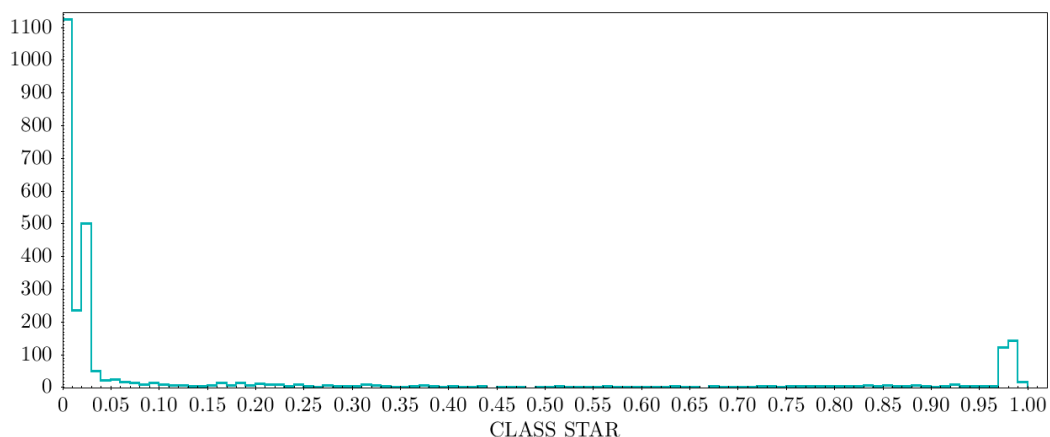


**Figure 3.6:** A histogram of CLASS\_STAR for the 2633 showing there is a clear separation between galaxies and stars. Anything above 0.97 was considered to be a star and used to create a subset of candidate that were ready for visual inspection.

Figure 3.6 shows a histogram of CLASS\_STAR for the 2633 sources. As explained, the sources near the lower end of the x axis are most likely galaxies and anything near 1.0 is most likely to be a star. There is a clear split between the two and so it was assumed that anything above 0.97 in figure 3.6 is a star.

A subset was created with these parameters and finally there were 281 potential metal-poor candidates that ready for visual inspection.

# 4

## Final Candidates

### 4.1 Visual Inspection

I visually inspected the 281 potential metal-poor candidates using high resolution ACS science image cutouts from the NASA/IPAC infrared science archive after inputting a file that had the RA and DEC of the candidates. Each object was given an ID based on RA and DEC starting with RUBY-1.

I chose a conservative cut, rejecting any source with a feature that appeared extended, using SAOIMAGEDS9 astronomical software (Joye & Mandel, 2003) to open the ACS fits files. Due to the application of CLASS\_STAR, anything too extended was removed in section 3.5, hence, the difference between stars and non-stars was not so obvious. DS9 has tools to manipulate images so potential structures before unseen can be revealed.

I explored different imaging scalings in order to ensure the selections were as accurate as possible. Figures 4.1 and 4.2 show examples of metal-poor candidates (with their RUBY-ID) that have been classified as galaxies/non-stars and stars respectively.

Upon completion of the visual inspection, 165 sources were deemed to be potential metal-poor stars.

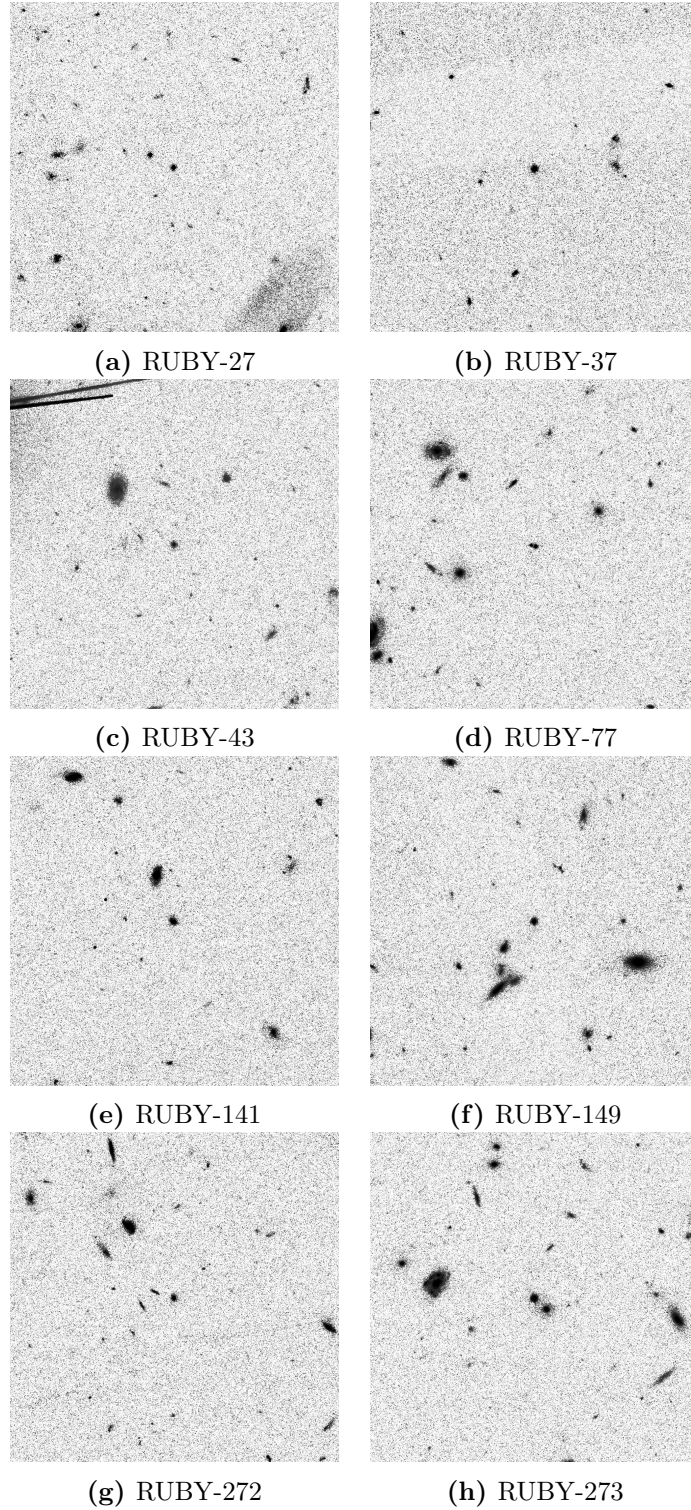


**Figure 4.1:** High resolution ACS images of a sample of candidates identified as galaxies/non-stars. The images were taken from NASA/IPAC Infrared Science Archive and have a size of  $15'' \times 15''$ .

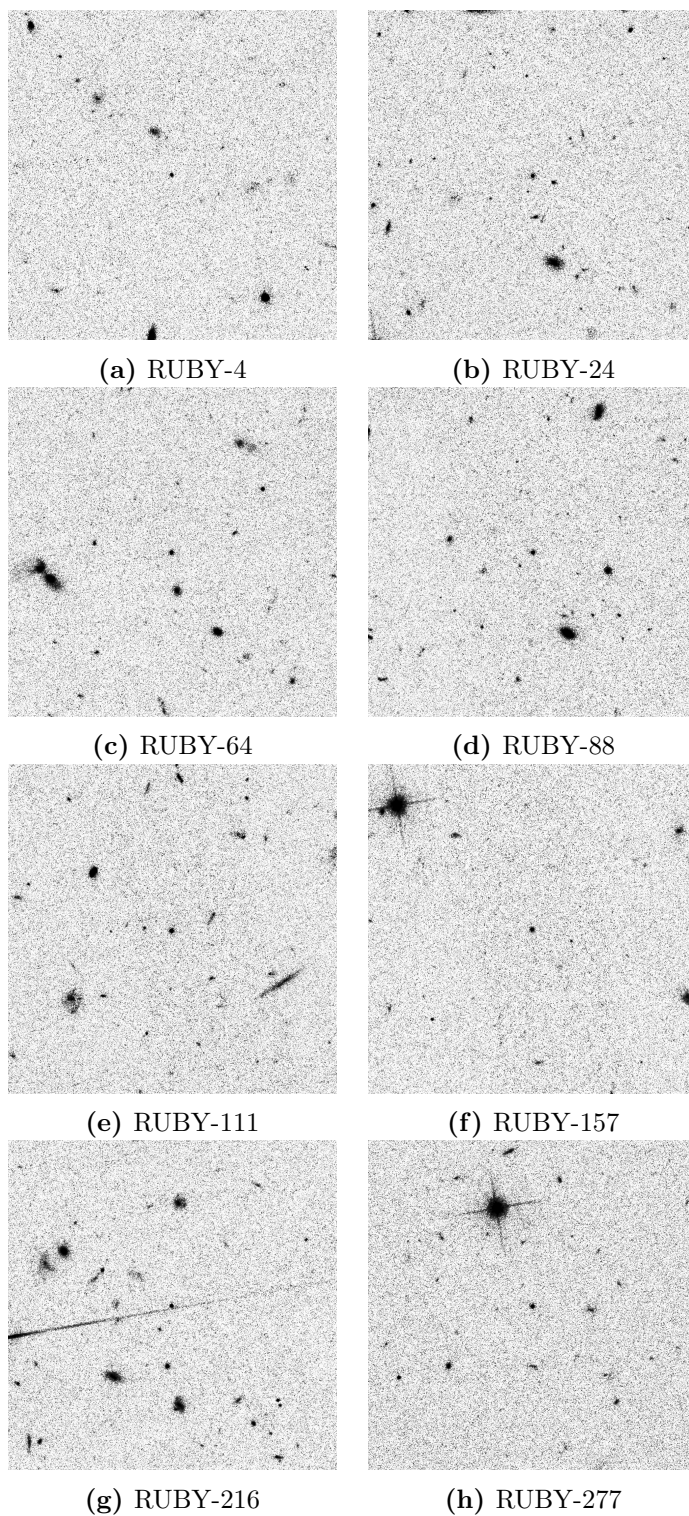


**Figure 4.2:** High resolution ACS images of a sample of candidates identified as stars. The images were taken from NASA/IPAC Infrared Science Archive and have a size of  $15'' \times 15''$ .

# 5

## Using simulated stellar spectra to estimate metallicities

The POLLUX database contains synthetic stellar spectra and was created at the university of Montpellier in France (Palacios et al., 2010). The following sections will go through how I used 102 theoretical spectra from the POLLUX database to compute magnitude values for multiple filter profiles, which I then used to estimate metallicities of the 165 candidate metal-poor stars.

### 5.1 Calculating Magnitudes

I used 102 theoretical stars ranging from F- to M-types with known integer metallicities of 0 to -5, to estimate magnitudes in the *NB392*, *g*, *u* and *i* filters, the full list of spectral types, along with their temperatures are presented in table 5.1.

I made sure there were at least three types of each spectral type, bar M-type stars because POLLUX only had one M star available. These values will help with number density and metallicity calculations later on as well as classifying the candidate metal-poor stars into spectral classes.

The filter profiles (Rodrigo et al., 2012) are given in fractional units such that the value is always between 0-1. I interpolated the filter profiles to a common

Spectral Type	Temperature (K)
A	8000
	7750
	7500
F	7250
	7000
	6750
	6500
	6250
G	6000
	5750
	5500
	5250
K	5000
	4500
	4000
	3700
M	3500

**Table 5.1:** Spectral types and temperatures of the synthetic spectra downloaded from the POLLUX database, all of which had spectra ranging from integer metallicities of 0 to -5 giving a total of 102 POLLUX spectra to work with.

wavelength axis as the POLLUX spectra. This was to ensure the wavelengths of the synthetic spectra matched the given wavelengths of the filter profiles.

After the interpolation I convolved the filter profiles with one of the stellar spectra which produced an observed flux in a given filter. Essentially, multiplying the spectrum by the filter transmission at each wavelength. The convolved spectrum was then integrated and divided by the full width half maximum (FWHM) of each filter making sure units were consistent. The range of wavelengths, effective wavelength and the FWHM value for each filter used can be found in Table 5.2.

In order to ensure all units are consistent throughout, I chose the  $AB$  magnitude system. The equation for  $AB$  magnitude is shown:

$$M_{AB} = -2.5 \log_{10} f_\nu (\text{erg s}^{-1} \text{ cm}^{-2} \text{ Hz}^{-1}) - 48.60 \quad (5.1)$$

Filter	$\lambda$ (Å)	$\lambda_{eff}$ (Å)	FWHM (Å)
<i>NB392</i>	3786 - 4094	3917	53.63
<i>u</i>	3020 - 4540	3823	528.7
<i>g</i>	3790 - 5667	4780	1155
<i>i</i>	6720 - 9170	7641	1395

**Table 5.2:** Summary of the range of wavelengths, effective wavelengths and the FWHM of the filters used in this study, all reported in Å

the previous steps gave the flux density in  $f_\lambda$  units but the values should be in  $f_\nu$  units. In the *AB* magnitude system, the two have this relation:

$$f_\nu = \left( \frac{\lambda^2}{c} \right) \times f_\lambda \quad (5.2)$$

where  $f_\nu$  is the flux density per unit frequency,  $f_\lambda$  is the flux density per unit wavelength.  $\lambda$  is the wavelength of the filter and  $c$  is the speed of light in a vacuum. The previous steps were repeated for the filters shown in table 5.2 and for all 102 synthetic spectra.

The flux densities calculated should have been equivalent to luminosity densities *i.e.* they are the flux densities you would measure if you were right next to the star. However, POLLUX uses arbitrary flux units, so the flux values at this point needed to be converted to meaningful values. To do this I used a POLLUX spectrum of a sunlike star and integrated the flux values with respect to the wavelengths and divided by the luminosity of the Sun ( $3.846 \times 10^{33}$  erg/s) to get a scaling factor. The POLLUX spectra was multiplied by the scaling factor and this ensured all the flux density values were as if they had been measured from the surface of the star.

From this I was able to estimate the absolute magnitudes and colours in *u*, *g*, *i* and *NB392*. The average magnitudes in *NB392* for each spectral type are in Table 5.3 and will be used later for number density estimations in section 6.1:

Spectral Class	Average Absolute Magnitude ( $M_{NB392}$ )
A	-0.51
F	0.43
G	2.04
K	5.87
M	8.92

**Table 5.3:** The average magnitude values in the *NB392* filter for each spectral class relevant to this study calculated for 102 POLLUX spectra.

## 5.2 Correlation Between g-i and Temperature

As explained in section 2,  $g - i$  is the most sensitive colour I was able to use for determining the temperature of medium and low-mass stars due to the difference of peaks of the two filters.

The correlation between  $g - i$  colours and temperature can be evaluated by plotting a graph of temperature vs  $g - i$  for the synthetic spectra as shown in figure 5.1.

I wanted to determine a functional form for this relation and fit it with a polynomial. I evaluated 3 different ways of determining which order of polynomial would be the best choice: reduced  $\chi^2$ , Akaike information criterion (AIC) and Bayesian information criterion (BIC).

WARP did not attempt to select an optimal polynomial order and chose a 5th-order polynomial which resulted in some overfitting. Overfitting is when a statistical model fits too closely or exactly to a specific set of data, and therefore is only useful to that data set. This means the model will fail to fit to unseen data, and will for the purposes of this thesis, not provide accurate spectral type estimates, hence it is important to avoid overfitting.

In figure 5.2a the log of the reduced  $\chi^2$  value was plotted against the order of polynomial and it seems like there is not much difference between a 3rd and 7th order polynomial. This plot does not account for the fact that reduced  $\chi^2$  will almost always go down as you add more free parameters, and so does not indicate when overfitting has occurred. AIC and BIC attempt to exclude overfitting in slightly different ways, it is evident by figures 5.2b and 5.2c that both are slightly

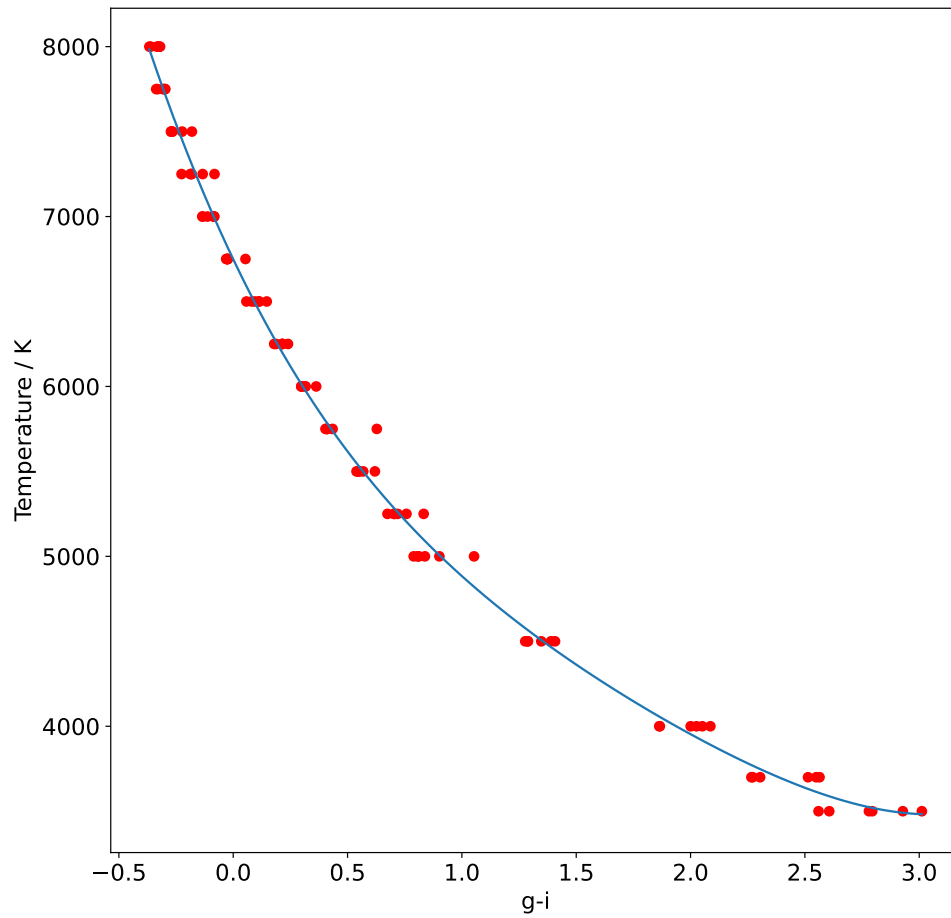


**Figure 5.1:** A plot of the temperature of the 102 synthetic spectra vs their  $g - i$  colour to show the correlation between the two parameters fitted with a curve of best fit described by the fourth-order polynomial shown in equation 6.3.

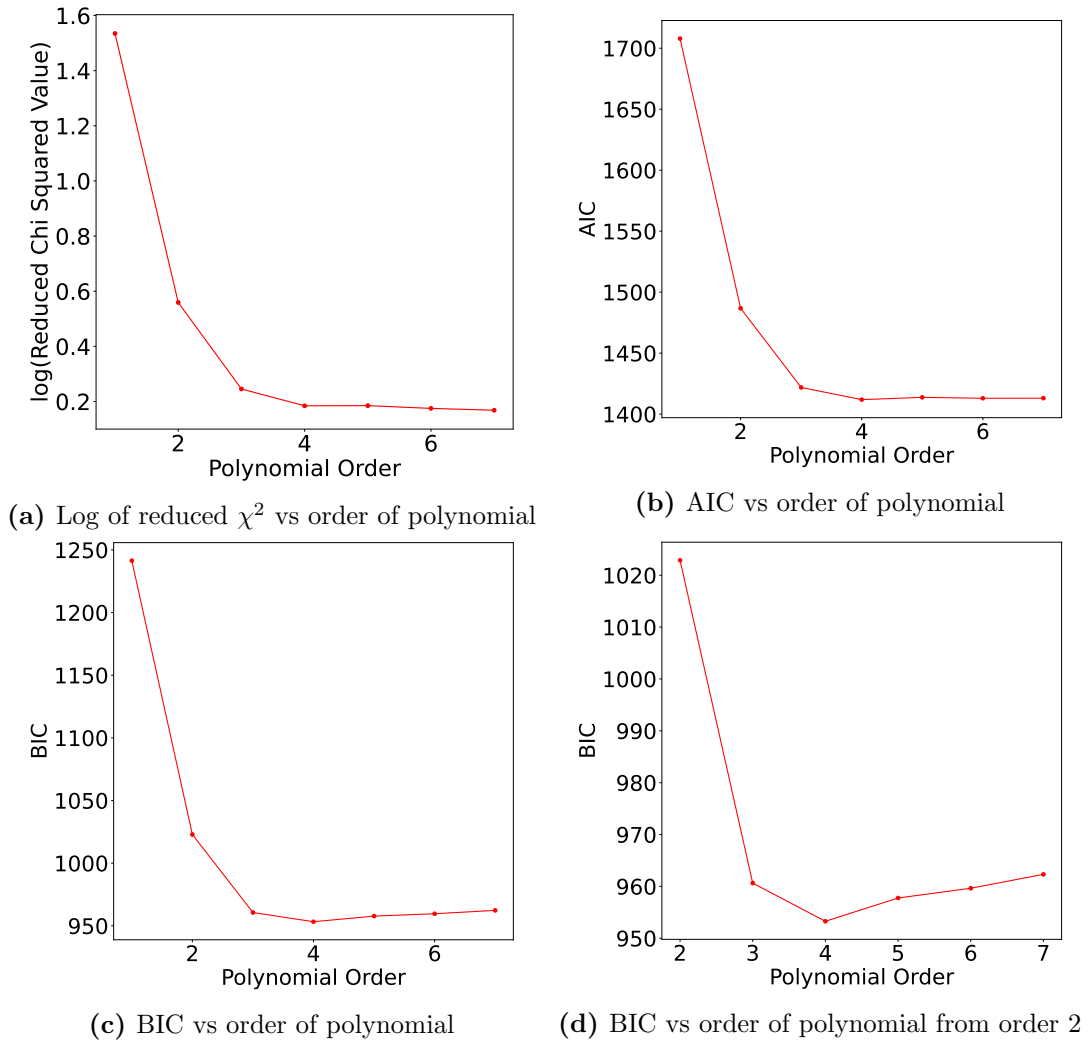


**Figure 5.2:** Plots of the reduced  $\chi^2$  AIC and BIC values vs polynomial order with 5.2d showing a zoomed in version of the BIC plot to show that the optimal order of polynomial is 4.

more useful at distinguishing statistical power than straight reduced chi<sup>2</sup> and a zoomed in version of the BIC plot shown in figure 5.2d shows clearly that fitting figure 5.1 with a 4th order polynomial is the best.

This fit was unweighted because in the simulated data no uncertainties are reported and was used to create figure 5.1, however the fit itself will have uncertainties.

Equation 5.3 shows the full fourth order polynomial used to fit the data and the curve of best fit is shown in figure 5.1.

$$T = 55.85(g-i)^4 - 414.18(g-i)^3 + 1318.89(g-i)^2 - 2825.51(g-i) + 6748.78 \quad (5.3)$$

$$T = A(g-i)^4 + B(g-i)^3 + C(g-i)^2 + D(g-i) + E \quad (5.4)$$

where the values for the coefficients and uncertainties are given in Table 5.4. The

Coefficient	Fitted Value
<i>A</i>	55.85 ± 16.06
<i>B</i>	-414.18 ± 80.10
<i>C</i>	1318.89 ± 113.31
<i>D</i>	-2825.51 ± 42.86
<i>E</i>	6748.78 ± 15.48

**Table 5.4:** Coefficient values of the fitted data and the reported uncertainties for 5.3.

uncertainties in each coefficient are reported from the diagonals for the covariance matrix from the fit (*i.e.*, ignoring the cross terms).

Using equation 6.3 each metal-poor candidate was classified into spectral classes defined by the temperature ranges in table 5.5, the results of which are reported in table 5.6.

As predicted most of the metal-poor stars are either F G or K. Due to the fact that only AFGK stars and one M star were used to calculate magnitudes, the  $g - i$  values are only accurate for stars with  $-0.37 < g - i < 3.01$  as these

## 5.2 Correlation Between $g-i$ and Temperature

Spectral Class	Temperature (K)	$g-i$	MS Lifetime (yrs)
O	>30000	<-2.60	$\approx 5 \times 10^6$
B	11000 - 30000	-1.32 to -2.60	$\approx 7.5 \times 10^7$
A	7500 - 11000	-0.227 to -1.32	$\approx 2 \times 10^9$
F	6000 - 7500	0.296 to -0.227	$\approx 1.2 \times 10^{10}$
G	5200 - 6000	0.666 to 0.296	$\approx 2 \times 10^{10}$
K	3500 - 5200	2.96 to 0.666	$\approx 2 \times 10^{11}$
M	<3500	>2.96	$\approx 2 \times 10^{12}$

**Table 5.5:** A table of spectral classes with their corresponding temperatures and  $g-i$  values, with average Main Sequence lifetimes adapted from (CSIRO, 2022)

Spectral Class	Number of sources
O	0
B	0
A	2
F	10
G	82
K	68
M	3

**Table 5.6:** A table showing the number of metal-poor candidates for each spectral class

were the smallest and largest  $g - i$  values for the available data. Therefore, the extrapolations will be less accurate for O and B-type stars according to table 5.5.

Because the  $g - i$  values extend down to the M-type star region, the estimates for these type of stars will be more accurate than those from WARP. However, only one M-type star was used for all metallicities and so it must be stressed again that the extrapolations are higher and so the confidence will be lower.

As depicted in table 5.6, there are no O and B-type stars in the potential candidates. WARP did not include a K or M-type star in their construction of the colour-colour plot, therefore the inclusion of these in my work means the estimates of metallicities for lower mass stars are relatively more accurate.

### 5.3 Colour-Colour Plots

As a reminder, accurate estimates for metallicities of the metal-poor stellar sources is the main aim. At this point in the investigation I had observed-colours, including narrow-band colours, plus, from the section above, synthetic stellar spectra with simulated-observed colours. With these I produced a colour-colour plot for the 102 synthetic stars which was created to show how metallicity is spread in relation to spectral type.

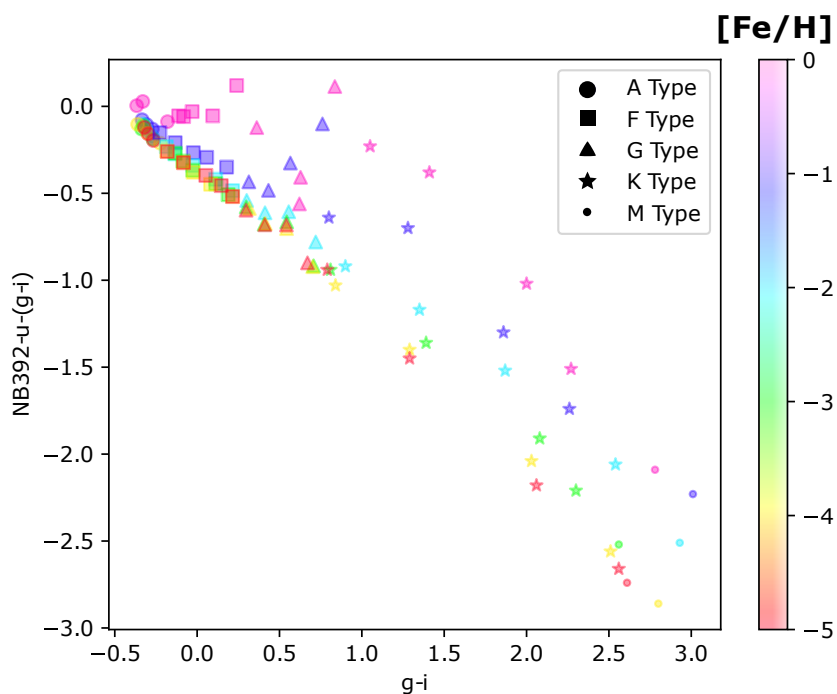


**Figure 5.3:** A colour-colour plot illustrating the separation between metallicities of 102 AFKM synthetic spectra from POLLUX that each have integer metallicities 0 to -5. The axes are  $NB392 - u - (g - i)$  vs  $g - i$ .

I used the approach WARP took and created a colour-colour plot where  $NB392 - u - (g - i)$  was used as the y-axis. This is because a single colour y-axis created a similar pattern but it was harder to distinguish between the various low metallicities. Therefore, I chose to plot the data this way as it presented the cleanest separation between metallicities, particularly at low metallicity, which is what this study is most interested in.

As explained in the section above, it is illustrated in figure 5.3 how the  $g - i$  values are only accurate for stars with  $g - i > -0.37$  with cluster of seemingly indistinguishable stars in the top left of the plot. There is also evidence of separation between the metallicities and at lower metallicities the sources become less and less distinguishable, even with the y-axis being the difference of two colours. This makes sense because as depicted in figure 1.4 as the metallicity decreases the CaHK absorption decreases, and so this effect can be seen with the small cluster in the bottom right corner of the figure especially.

In an attempt to slightly overcome this intrinsic property of CaHK absorption I created another colour-colour plot, this time with the y-axis being  $NB392 - g - (g - i)$ , this is shown in figure 5.4

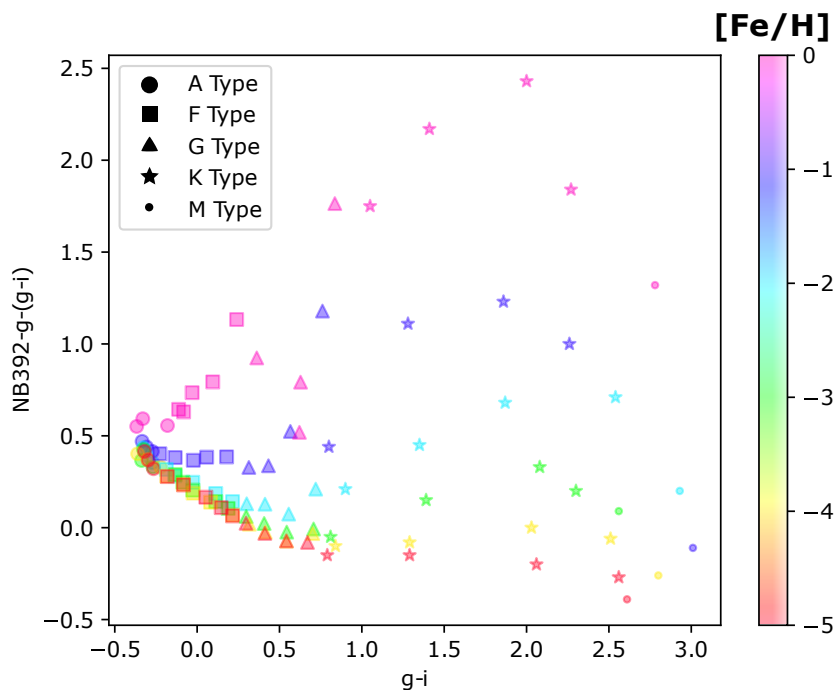


**Figure 5.4:** A colour-colour plot illustrating the separation between metallicities of AFGK synthetic spectra from POLLUX that each have integer metallicities 0 to -5. The axes are  $NB392 - g - (g - i)$  vs  $g - i$ .

Figure 5.4 is slightly better at discerning between lower metallicity stars, such as the EMP, UMP and HMP stars. Evidence for this is that the same cluster of

stars in the bottom right figure are now relatively separated and there is more separation of metallicities in general.

Ideally, I wanted to use this colour-colour plot to calculate the metallicity of the candidate metal-poor sources, however, as WARP pointed out; it was difficult to overlay the candidate sources as the spread was too small to do any real analysis.

Therefore I used figure 5.4 to create a grid interpolating between the simulated values in the form of a metallicity heat map, which is the basis of the next section.

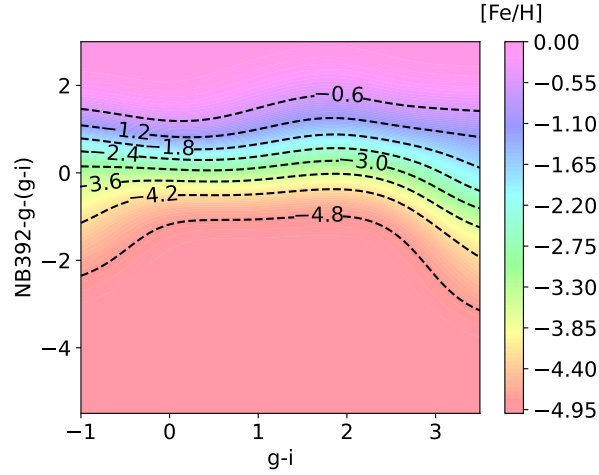
## 5.4 Metallicity Heatmap

To construct the heatmap, firstly I split the values from figure 5.4 into a 100x100 grid point, based on interpolation of the metallicities and colours of the synthetic stars. This allowed corresponding y-values to be estimated and I assigned the metallicities as an array in the z-axis.

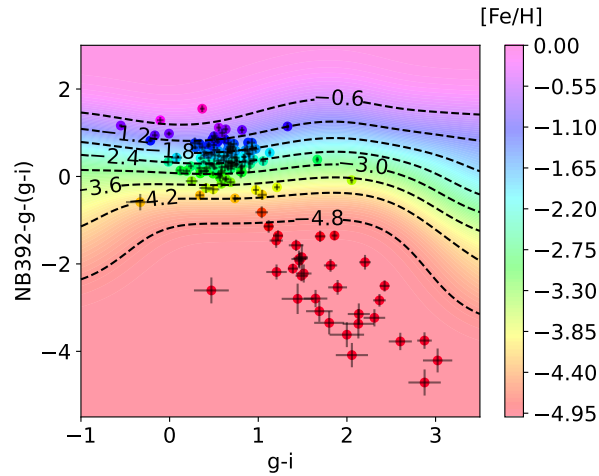
Due to only having 102 synthetic stars the sample was sparse and metallicities are trying to be assigned to a 10,000 grid point. This means the interpolation may create artificial features and blank spaces in the heat map. In order to remove these, and ensure smooth transitions between metallicities, I applied a Gaussian smoothing function to the metallicity grid, with  $\sigma = 8$  grid points, and when the filter overlaps a border, the input is extended by replicating the last pixel. This smoothing also allows me to extend the grid to colours beyond those covered in the simulations.

The resultant heatmap is shown in figure 5.5a and was created in PYTHON using the following packages: SCIPY, ASTROPY, MATPLOTLIB AND NUMPY, and can be used as an accurate and reproducible way of estimating the metallicities of the candidate metal-poor stars.

Figure 5.5b shows the heatmap with the candidate stars plotted. I used the heatmap to assign metallicities to the candidate stars, linearly interpolating between grid points where necessary.



(a) Colour difference  $NB392 - g - (g - i)$  versus  $g - i$  colour of observed stars in the COSMOS field. The colourised gradient is a metallicity map based on simulated stellar spectra and colours.



(b) Colour difference  $NB392 - g - (g - i)$  versus  $g - i$  colour of observed stars in the COSMOS field. The colourised gradient is a metallicity map based on simulated stellar spectra and colours. The 165 candidate metal-poor stars are overlaid with the colour of the sources corresponding to metallicity values along with error bars.

**Figure 5.5:** Plots of the metallicity heatmap without and with candidate metal-poor stars.

### 5.4.1 Approximating uncertainties on metallicities

A bootstrap method was implemented in calculating the errors for each candidate star. Each colour on the x and y axis used had an error for every source. I created a Gaussian distribution of each colour error and assumed this represented the intrinsic uncertainty for each axis. I then calculated a metallicity using each sampling from that distribution. Drawing the sample data in this way allowed me to calculate a median and standard deviation for the metallicity. The median was assigned as the metallicity value in the z axis over the mean value as the median is less likely to be affected by outliers. The standard deviation describes the error on this point.

Tables A.1 to A.6 shows the values of metallicity and the corresponding uncertainties for every candidate star, as derived using this heatmap method.

The uncertainties on the metallicities range from  $2.52 \times 10^{-6}$  to  $5.25 \times 10^{-1}$  with a typical value of  $1.80 \times 10^{-1}$ . For those candidates below -3 the typical uncertainty is  $2.27 \times 10^{-2}$ .

By getting more POLLUX spectra, I attempted to increase the data for the lower metallicities so that the estimates were more accurate in comparison to WARP. Many of the sources lie between metallicities of 0 and -1.5. This is in line with what WARP found. This is also expected as most stars are have metallicities close to the Sun as they are Pop I stars and Pop II stars are rarer, older and more metal-poor.

Via this method, 16 stars were found to be EMP and 38 were found to be UMP. Although these are just estimates, the lower metallicity candidates sit firmly within the red shaded region of figure 5.5b and the error bars suggest that even if these estimates are wrong, the candidate stars will still be around that metallicity. The only way of getting accurate metallicity values is by analysing the spectra of the individual EMP and UMP candidates. This suggests that I could potentially add to the sample because I could accept stars where the uncertainties in the colours are higher, which would have given me more potential metal-poor candidates. However, the application of CLASS\_STAR was thought to be necessary due to 2633 sources being a large sample to visually inspect.

# 6

## Number Densities and Distance Estimates of Metal-Poor Stars

### 6.1 Number Densities

As mentioned in section 1.4 number densities of metal-poor stars can be used to help constrain the Initial Mass Function, and explore stellar evolution and galactic structure.

This section focuses on investigating the number densities of the 165 candidate metal-poor stars identified in this study so they can be compared to the findings of other studies.

The area of sky observed according to Sobral et al. (2017) is 1.43 deg<sup>2</sup> and from section 3.2 it was asserted that 25 was the limiting magnitude ( $m_l$ ) for the *NB392* filter. I used the average absolute magnitude values ( $M$ ) for *NB392* shown in table 5.3 calculated from POLLUX and equation 7.1 to calculate limiting distances ( $D_l$ ).

$$D_l = 10^x \text{ where } x = \frac{m_l - M + 5}{5} \quad (6.1)$$

I then used equation 6.2 used to calculate the volumes for each spectral type. This uses the fraction of the total sky's surface area ( $A_{obs}/A_{sky}$ ) to find the ob-

served volume. Table 6.1 shows the average magnitude values and volumes.

$$V_{obs} = \frac{4\pi D_l^3}{3} \frac{A_{obs}}{A_{sky}} \quad (6.2)$$

Spectral Class	Average Absolute Magnitude ( $M_{NB392}$ )	$V_{obs}$ ( $\text{pc}^3$ )
A	-0.51	$2.93 \times 10^{14}$
F	0.43	$8.02 \times 10^{13}$
G	2.04	$8.64 \times 10^{12}$
K	5.87	$4.39 \times 10^{10}$
M	8.92	$6.45 \times 10^8$

**Table 6.1:** Average  $M_{NB392}$  values for all relevant spectral classes as determined from 102 synthetic stellar spectra and their corresponding observed volumes.

The number densities were calculated using the volumes from table 6.1 and the number of stars that were obtained per spectral type. The 165 sources were grouped by spectral type, metallicity and then the number of sources in each group were summed and divided by the surveyable volume for each spectral type. This gives the number density per metallicity per spectral type. I used a Poisson distribution on the number of stars in each bin of spectral type to estimate errors in number density. The error in  $g-i$  comes from the size of  $g-i$  for each spectral type.

Table 6.2 gives a summary of the number densities and sources per spectral for each metallicity and figure 6.1 gives a visual representation of this information.

The surveyed volume for A-type stars is the largest and there are only 2 A type stars identified, hence the low number density. Although there is only 1 M-type star identified the surveyed volume is 6 orders of magnitudes smaller than that for A type stars, hence the relatively high number density.

The number densities of F,G and K-type stars are  $(1.50 \pm 0.81) \times 10^{-13} \text{ pc}^{-3}$ ,  $(7.64 \pm 1.89) \times 10^{-12} \text{ pc}^{-3}$  and  $(1.91 \pm 0.34) \times 10^{-9} \text{ pc}^{-3}$  respectively. Overall the number densities follow the same pattern as reported in Bovy (2017) with A having the smallest number and density and K having the largest. A higher abundance of the latter was to be expected due to K type stars having longer lifetimes than F and G stars. This pattern was also found by WARP.

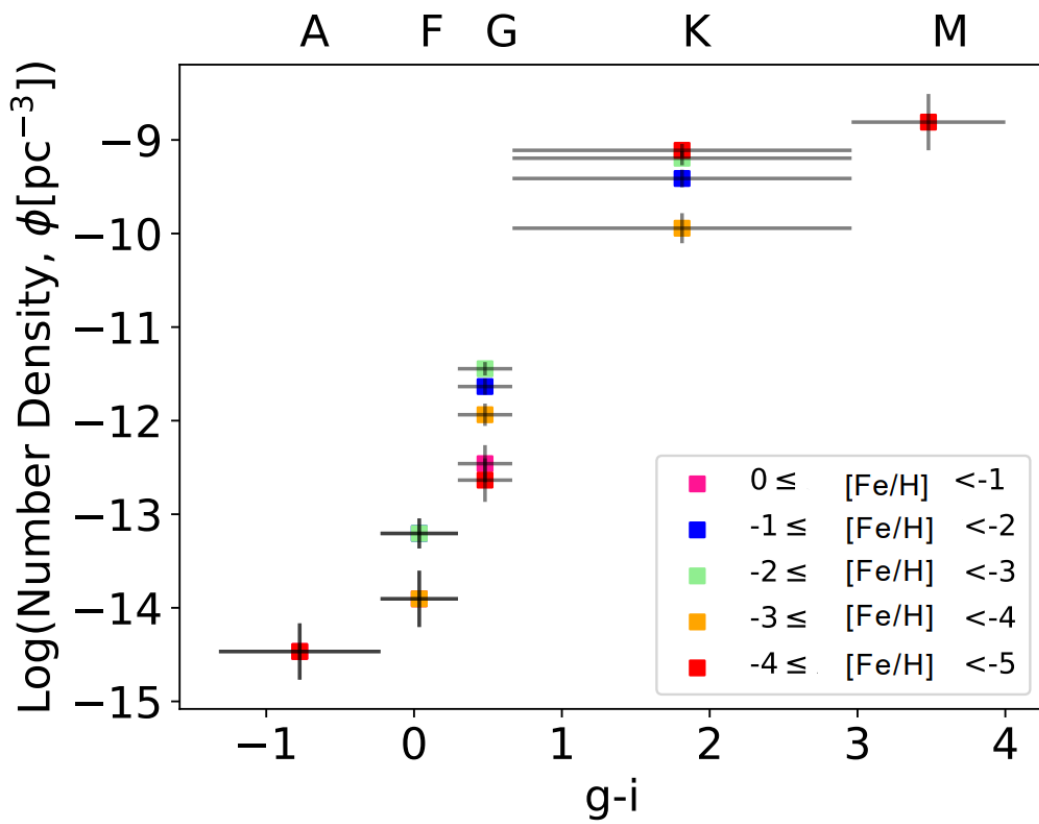


**Figure 6.1:** A visual representation of the information displayed in Table 6.2 which are the number densities per spectral type for each metallicity.

Spectral Type	[Fe/H]	Number Density ( $pc^{-3}$ )	Number of sources
A	0	$3.41(\pm 3.41) \times 10^{-15}$	1
	-1		0
	-2		0
	-3		0
	-4	$3.41(\pm 3.41) \times 10^{-15}$	1
	-5		0
F	0	$1.25(\pm 1.25) \times 10^{-14}$	1
	-1	$6.23(\pm 2.79) \times 10^{-14}$	5
	-2	$6.23(\pm 2.79)(\pm 3.41) \times 10^{-14}$	5
	-3	$1.25(\pm 1.25) \times 10^{-14}$	1
	-4		0
	-5		0
G	0	$3.47(\pm 2.00) \times 10^{-13}$	3
	-1	$2.31(\pm 0.52) \times 10^{-12}$	20
	-2	$3.59(\pm 0.64) \times 10^{-12}$	31
	-3	$1.16(\pm 0.37) \times 10^{-12}$	10
	-4	$2.31(\pm 0.16) \times 10^{-12}$	2
	-5		0
K	0		0
	-1	$3.87(\pm 0.94) \times 10^{-10}$	17
	-2	$6.38(\pm 1.21) \times 10^{-10}$	28
	-3	$1.14(\pm 0.51) \times 10^{-10}$	5
	-4	$7.74(\pm 1.33) \times 10^{-10}$	34
	-5		0
M	0		0
	-1		0
	-2		0
	-3		0
	-4	$1.55(\pm 1.55) \times 10^{-9}$	1
	-5		0

**Table 6.2:** Summary of number densities per spectral type for each metallicity and the number of sources.

34 K-type UMP stars were identified, due to the limitations of the heatmap *i.e.* a lack of data for K and M-type stars at their respective masses, these are likely upper estimates for the number of actual K stars.

### 6.1.1 Expected Number Densities of EMP and UMP Stars

Table 6.2 can be used to examine the rare population of EMP and UMP stars.

Via the methodology described in Magg et al. (2019). I calculated the expected number densities of EMP and UMP stars.

I assumed that all EMP and UMP stars are located in the halo of the Milky Way, simulations by Starckenburg et al. (2017) back this as they found that the majority of UMP stars are found in the stellar halo.

Bell et al. (2008) estimated the mass of the stellar halo to be  $\approx 10^9 M_\odot$ . I used an average stellar mass of  $M_* = 1M_\odot$ , this is higher than the one used by Magg et al. (2019) because as mentioned in section 1.4, the IMF of of Pop III stars is top heavy and the POLLUX spectra all had masses of  $1M_\odot$ . Youakim et al. (2017) estimate that 1/800 stars in the halo are EMP and 1/8000 stars are UMP. So I estimate the number of EMP ( $N_{EMP}$ ) and UMP ( $N_{UMP}$ ) stars in the halo of the Milky Way:

$$N_{EMP} = \frac{M_{halo}}{800M_*} \approx 1.25 \times 10^6 \quad (6.3)$$

$$N_{UMP} = \frac{M_{halo}}{80,000M_*} \approx 1.25 \times 10^4 \quad (6.4)$$

According to Deason et al. (2019), past  $\approx 100$  kpc there is very little halo mass and so the radius of the halo of the Milky Way is assumed to be  $\approx 100$  kpc. Whilst the Milky Way isn't spherical, metal-poor stars are most commonly found in the halo, which can be reasonably approximated as spherical. So I was able to calculate the volume to be  $V_{halo} \approx 4.19 \times 10^{15} \text{ pc}^3$ .

$$n_{i, expected} = \frac{N_i}{V_{halo}} \quad (6.5)$$

Using equation 7.5 I found the expected number densities of EMP and UMP, these values as well as the observed number densities are shown in tables 6.3 and 6.4:

Although the values for number densities are approximations and will have large uncertainties according to Magg et al. (2019), the observed number densities for EMP stars are closer to the expected number densities and are even of the same

Metallicity Classification	Expected ND ( $pc^{-3}$ )	Observed ND (this work) ( $pc^{-3}$ )
EMP	$2.98 \times 10^{-10}$	$(1.15 \pm 0.51) \times 10^{-10}$
UMP	$2.98 \times 10^{-12}$	$(2.33 \pm 1.68) \times 10^{-9}$

**Table 6.3:** A comparison of the expected number density values for EMP and UMP stars discovered in this investigation to the observed number densities.

Metallicity Classification	Expected ND ( $pc^{-3}$ )	Observed ND (WARP) ( $pc^{-3}$ )
EMP	$4.96 \times 10^{-10}$	$(4.6 \pm 2.6) \times 10^{-11}$
UMP	$4.96 \times 10^{-12}$	$(3.1 \pm 2.1) \times 10^{-11}$

**Table 6.4:** A comparison of the expected number density values for EMP and UMP stars discovered WARP's investigation to their observed number densities.

magnitude in comparison to WARP's observed number densities. The observed number density for UMP stars however is significantly larger than the expected number density for these types of stars. WARP got a lower observed number density for UMP stars and I got a higher one.

This can be attributed to the approximations in the calculations leading to large uncertainties. In addition to this, the ability to accurately estimate metallicity values decreases with decreasing metallicity and so it is possible many stars classified as UMP may either be lower or higher in metallicity. Hence the need for further investigations using detailed spectra to obtain accurate metallicity values.

## 6.2 Estimated Stellar Distances

Distance estimates to the relevant metal-poor stellar candidates (*i.e.* potential UMP and EMP sources) can be calculated using a variation of equation 6.1. So far I have assumed the stellar candidates are all still on their main sequence (MS).

To investigate whether this is true I estimated the distances of each stellar candidate as if it were a MS star ( $d_{MS}$ ) or a red giant ( $d_{RG}$ ). The distances are tabulated below in tables 6.5 and 6.6.

RA	Dec	$NB392$ ( $m$ )	$NB392$ Error	Avg Absolute ( $M_{NB392}$ )	[Fe/H]	Spectral Class	$d_{MS}$ (kpc)	$d_{MS}$ Error	$d_{RG}$ (kpc)	$d_{RG}$ Error
149.48802	1.92434	24.47	0.13	8.92	-4.96	K	52.58	0.13	627.94	0.13
149.48916	2.56823	24.99	0.15	5.87	-4.99	M	16.37	0.15	319.58	0.15
149.49674	2.05109	24.38	0.28	5.87	-4.99	K	50.23	0.28	343.65	0.28
149.50241	2.65866	24.96	0.14	5.87	-4.98	K	65.78	0.14	364.60	0.14
149.50626	2.03002	23.81	0.17	5.87	-4.99	K	38.71	0.17	381.65	0.17
149.52158	2.33101	24.57	0.13	5.87	-4.99	K	54.86	0.13	398.66	0.13
149.55324	2.25843	24.32	0.10	5.87	-4.99	K	48.89	0.10	399.28	0.10
149.62959	1.95105	24.39	0.12	5.87	-4.87	K	50.61	0.12	401.55	0.12
149.75593	2.64615	23.68	0.08	5.87	-4.99	K	36.49	0.08	436.94	0.08
149.78503	2.37329	24.70	0.10	5.87	-4.99	K	58.37	0.10	438.43	0.10
149.79153	1.63663	24.48	0.15	5.87	-4.99	K	52.74	0.15	438.63	0.15
149.79751	1.81818	24.36	0.11	5.87	-4.99	K	50.00	0.11	447.65	0.11
149.80615	2.52362	24.73	0.10	5.87	-4.99	K	59.09	0.10	460.49	0.10
149.82463	2.43671	24.61	0.09	5.87	-4.99	K	55.93	0.09	465.07	0.09
149.86779	1.69358	24.20	0.12	5.87	-4.99	K	46.39	0.12	470.96	0.12
149.88051	1.92697	24.21	0.09	5.87	-4.93	K	46.55	0.09	473.15	0.09
149.97496	2.44653	24.47	0.07	5.87	-3.71	K	52.43	0.07	476.52	0.07
150.03676	1.70872	24.59	0.17	5.87	-4.99	K	55.47	0.17	476.72	0.17
150.03696	1.70062	24.00	0.10	5.87	-3.96	K	42.33	0.10	487.71	0.10
150.05048	1.69508	24.48	0.15	5.87	-4.99	K	52.60	0.15	493.88	0.15
150.06614	1.81631	24.53	0.12	5.87	-4.99	K	53.96	0.12	495.27	0.12

Table 6.5: Summary of the 41 EMP and UMP stellar candidates along with their estimated distances in kpc. *cont.*

RA	Dec	$NB392$ ( $m$ )	$NB392$ Error	Avg Absolute ( $M_{NB392}$ )	[Fe/H]	Spectral Class	$d_{MS}$ (kpc)	$d_{MS}$ Error	$d_{RG}$ (kpc)	$d_{RG}$ Error
150.07312	1.73132	24.91	0.23	5.87	-4.99	K	64.30	0.23	495.47	0.23
150.15891	1.63061	24.87	0.10	5.87	-4.65	K	63.14	0.10	496.73	0.10
150.17366	2.83781	24.21	0.06	5.87	-3.86	K	46.57	0.06	497.97	0.06
150.18473	2.81810	24.91	0.10	5.87	-4.94	K	64.13	0.10	508.23	0.10
150.18832	1.85878	24.61	0.08	5.87	-4.99	K	55.91	0.08	516.70	0.08
150.19071	1.98188	24.84	0.09	5.87	-4.13	K	62.36	0.09	522.42	0.09
150.25679	2.85312	24.34	0.06	5.87	-3.56	K	49.38	0.06	525.92	0.06
150.27798	2.82779	24.60	0.08	5.87	-4.99	K	55.84	0.08	526.65	0.08
150.32814	2.46896	24.25	0.15	5.87	-4.99	K	47.53	0.15	526.77	0.15
150.38461	2.24301	24.01	0.10	5.87	-4.94	K	42.39	0.10	540.08	0.10
150.39146	2.81987	24.66	0.08	5.87	-4.99	K	57.34	0.08	549.79	0.08
150.42255	1.79053	24.76	0.07	5.87	-4.97	K	60.10	0.07	556.52	0.07
150.45925	2.71225	24.49	0.08	5.87	-4.99	K	52.87	0.08	566.08	0.08
150.46642	2.16429	24.77	0.08	5.87	-4.99	K	60.16	0.08	566.66	0.08
150.49149	2.36728	24.39	0.17	5.87	-4.99	K	50.59	0.17	577.17	0.17
150.50652	2.39706	24.81	0.25	5.87	-4.99	K	61.28	0.25	587.38	0.25
150.56291	2.25915	24.44	0.14	5.87	-3.00	K	51.78	0.14	594.73	0.14
150.62128	2.22613	23.52	0.06	5.87	-4.22	K	33.93	0.06	604.03	0.06
150.64109	2.24077	23.91	0.09	5.87	-4.99	K	40.52	0.09	605.62	0.09
150.66597	2.54960	24.02	0.08	5.87	-3.00	K	42.63	0.08	619.56	0.08

**Table 6.6:** Summary of the 41 EMP and UMP stellar candidates along with their estimated distances in kpc.

I achieved this by taking the apparent magnitudes ( $m$ ) of each stellar candidate through the *NB392* filter.

For  $d_{RG}$ , the red giant branch on figure 1.5 is relatively flat, so it is reasonable to estimate a constant absolute magnitude for it. (Karaali et al., 2012) reported many red giants to have an absolute magnitude of 1. Although figure 1.5 and (Karaali et al., 2012) used  $B - V$  colour, I can assume these colours will not be drastically different to the ones I am using as the B band is centred near 400nm instead of 392nm and  $V$  and  $g$  are also very similar.

For  $d_{MS}$  I again used the apparent magnitudes ( $m$ ) of each stellar candidate through the *NB392* filter. In addition to this I used tables 5.5 and 6.1, to assign the average absolute magnitude ( $M_{NB392}$ ) to each candidate star based on its spectral class. This then allowed me to calculate the distance of the sources in kpc.

Table ?? shows the information of the relevant 41 EMP and UMP candidates that are at a distance ( $d_{MS}$ ) of less than 66kpc.

As mentioned earlier radius of the halo of the Milky Way is assumed to be  $\approx 100$  kpc. This suggests all 41 UMP and EMP stars shown in Table ?? sit well within the halo, if approximated as main sequence stars. It is clear that if the metal-poor candidates are assumed to be red giants, they would be situated way out of the halo with the smallest distance being 319.58 kpc.

All candidates are K-type stars bar one and so according to figure 1.5 and using the main sequence life time estimates from table 5.5 it can be assumed they are all still on this stage of their evolutionary cycle.

# 7

## Metallicity Distributions

I used the number density estimates calculated in the previous section to create an MDF of the halo of the Milky Way shown in figure 7.1.

G and K-type stars on figure 7.1 exhibits a tail to the low metallicity end which is expected as discussed in section 1.4.1. The shape of the MDF for all spectral types follow a similar pattern to what is reported in the literature and the median  $[\text{Fe}/\text{H}]$  values of F, G and K type stars are -1.5, -2 and -2.5 respectively. F-type stars are modelled particularly well with the literature value of  $[\text{Fe}/\text{H}] = -1.6$  for the peak of the MDF.

Figure 7.1 also gives a visual representation of the rarity of metal-poor stars, particularly for F-type stars as there were no UMP F-type stars identified.

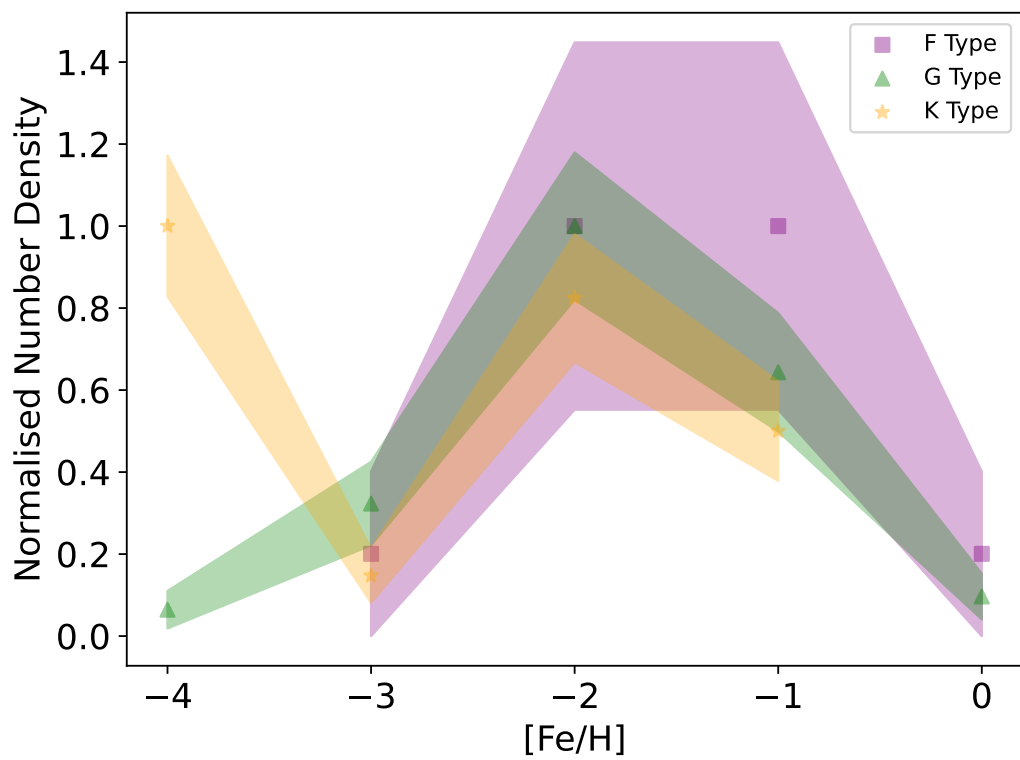


**Figure 7.1:** Metallicity distribution function for F, G and K type stars identified from the 165 metal-poor candidates

# 8

## Future work

CLASS\_STAR has been superseded by the SPREAD\_MODEL in SExtractor and it provides better performance by “making explicit use of the full, variable PSF model”, therefore in the future it is advised to use this classifier instead.

One of the original goals for this study was to use GAIA data to get distances to the candidate EMP and UMP stars to confirm whether or not they are in the halo and thus whether or not their fluxes/luminosities and colours are consistent with being main-sequence stars. 54 EMP and UMP candidate stars were identified in this study, and GAIA data was not able to be used to estimate distances for these candidates as the magnitude limit of the GAIA survey is  $G = 20.7$ , as can be seen in tables A.1 to A.5, every magnitude value is above this limit meaning it was impossible to cross reference the candidate stars with GAIA to obtain distances. This will be possible if future GAIA surveys can go fainter.

Obtaining spectra for the candidate EMP and UMP stars can confirm the findings. However, the metal-poor star candidates identified are too faint for the required confirmation spectroscopy, which is unfeasible with current instrumentation (e.g. on the VLT) and will be even be prohibitively expensive with a facility such as the E-ELT.

The POLLUX database contains a very limited bank of synthetic spectra. Most of the masses of stars were limited to  $1 M_{\odot}$  which is not representative of most spectral classes. Temperatures were also limited and there were only integer value metallicities below -3. This suggests the intrinsic inability to distinguish

---

between and therefore estimate metallicities for stars at lower metallicities can be further improved by obtaining synthetic spectra at lower metallicities.

# 9

## Conclusions

I used the CALYMHA (Sobral et al., 2017) catalogue containing 123,505 sources that were obtained via the INT/WFC surveying a  $1.43 \text{ deg}^2$  area of sky to probe the COSMOS field in an attempt to replicate and improve the work of Jenkins et al. (2019). The main goal of this study was to identify potential EMP and UMP star candidates in the halo of the Milky Way.

I cross matched the COSMOS and CALYMHA catalogues accepting the closest match between  $3''$ , this resulted in the RUBY catalogue of 94,591. Every subsequent step applies to this catalogue. I created a star-galaxy cut based on the assumption that stars have a redshift of zero and galaxies have a redshift of non-zero to provide a cut whereby everything above the line in figure 3.2 was considered to be a star. This cut was applied to the RUBY catalogue and sources with extreme magnitude values were removed resulting in 9871 sources. The estimated contamination and completeness at this stage were 12% and 85%.

Applying error limits in the x and y axis and a magnitude limit of 25 further reduced the number of sources to 2633. I plotted a histogram of CLASS\_STAR to further separate stars and galaxies based on the stellarity index and this resulted in 281 candidates that needed to be visually inspected. I used high resolution ACS images as well as tools in DS9 to identify a final selection of 165 metal-poor candidate stars. This shows the actual contamination of the sample was 41% and proves the earlier contamination value was just an estimate, but still useful for identifying a compromise between contamination and completeness.

---

A plot was produced of temperature vs  $g - i$  and using the correlation between these two I was able to classify stars based on the fourth-order polynomial describing the line of best fit. Most candidate stars had expected spectral types of F, G or K.

Using the POLLUX database I was able to obtain 102 theoretical spectra with complete integer metallicities of 0 to -5. Using these, I was able to estimate magnitudes values for the  $NB392$ ,  $g$ ,  $u$  and  $i$  filters. Using colour-colour plots I was able to identify that the best separation of metallicities in relation to spectral type was given by a colour-colour plot where the x axis is  $g - i$  and the y axis is  $NB392 - g - (g - i)$ . This study used more theoretical spectra than WARP and a colour-colour plot that gave a higher separation of metallicities therefore, this method is better at discerning between lower metallicities.

I then created a metallicity heatmap from the colour-colour plot and used it to estimate metallicity values for the candidate stars, via this method 16 stars were found to be EMP and 38 were found to be UMP. Out of the total 54 EMP and UMP stars, 41 were found to be at a distance of less than 66 kpc and thus assumed to be in the halo of the Milky Way.

The candidate F, G, and K-type stars found in this study had number densities of  $(1.50 \pm 0.81) \times 10^{-13} \text{ pc}^{-3}$ ,  $(7.64 \pm 1.89) \times 10^{-12} \text{ pc}^{-3}$  and  $(1.91 \pm 0.34) \times 10^{-9} \text{ pc}^{-3}$  correspondingly, which is consistent with the pattern described in the literature. The MDF of the candidate metal-poor stars shows that F-type stars peak around  $[\text{Fe}/\text{H}] = -1.5$ , which is close to the figure of  $[\text{Fe}/\text{H}] = -1.6$  reported in the literature.

# Appendix A

## Appendices

### A.1 Completeness and Contamination

Completeness is defined as the stars recovered in a sample over the total classified stars. The equation used to calculate this simple fractional representation is given by:

$$\text{Completeness} = \frac{\text{Recovered stars}}{\text{Total classified stars}} \quad (\text{A.1})$$

Using WARP's star galaxy cut an overall completeness of 75.3% was given which they then extrapolated as the completeness for the rest of the data. Using my cut the estimated completeness improved greatly to 84.7%

Inevitably some of the sample star population will be polluted by galaxies, in order to statistically measure this proportion the contamination must be calculated. Similarly to completeness, before contamination could be calculated, sources with extreme magnitude values had to be removed.

Equation 4.4 is used to calculate the fraction of contaminant galaxies on the stellar side of the cut

$$\text{Contamination} = \frac{\text{Pollutant galaxies}}{\text{Total classified sources}} \quad (\text{A.2})$$

WARP reported a contamination of 6.1% using their star-galaxy cut, this

is lower than the 11% obtained using my cut. However, there is always a balance between the two and since the completeness increased a lot more than the contamination the study was moved forward with the new cut.

The completeness and contamination values calculated for the star galaxy cut are provisional and the actual contamination was 41% due to 116 of the 281 candidates being classified as galaxies/non-stars. The overall completeness therefore was 59%.

## A.2 165 candidates summary

Tables A.1 to A.6 report a summary of the RA, DEC, magnitudes in *NB392*, *g*, *u* and *i* filters and [Fe/H] values with errors for the 165 metal poor candidates.  $\sigma_x$  and  $\sigma_y$  refer to the errors in the x and y values for each of the 165 metal-poor candidates displayed on figure 5.5b.

RA	DEC	NB392	$u$	$g$	$i$	[Fe/H]	$\sigma_x$	$\sigma_y$
150.64109	2.240	23.90	26.52	24.69	23.20	-4.99 ± 0.001	±0.067	±0.126
149.65951	2.512	24.04	24.79	24.96	25.29	-4.22 ± 0.304	±0.161	±0.188
150.07312	1.731	24.91	28.12	26.15	24.02	-4.99 ± 0.000	±0.177	±0.335
150.65062	1.634	24.31	24.88	24.17	23.92	-3.56 ± 0.261	±0.066	±0.094
150.14508	2.223	24.52	24.19	23.18	22.46	-1.75 ± 0.193	±0.032	±0.070
150.15891	1.630	24.87	25.90	24.65	23.61	-4.65 ± 0.157	±0.071	±0.135
150.20824	2.128	24.22	24.64	23.80	23.22	-3.55 ± 0.212	±0.046	±0.079
149.50143	2.100	23.85	25.89	25.99	25.52	-4.99 ± 0.007	±0.196	±0.296
150.34483	2.259	23.59	24.38	23.68	23.34	-4.21 ± 0.168	±0.044	±0.087
150.39146	2.819	24.66	27.65	25.80	24.16	-4.99 ± 0.000	±0.133	±0.198
150.45925	2.712	24.48	25.32	25.46	24.25	-4.99 ± 0.004	±0.115	±0.172
150.41411	2.678	24.30	24.11	23.43	23.04	-2.07 ± 0.238	±0.040	±0.081
150.06614	1.816	24.53	27.69	26.07	24.27	-4.99 ± 6.486	±0.169	±0.264
150.0344	2.348	24.88	24.83	23.44	22.59	-2.00 ± 0.230	±0.036	±0.092
149.82463	2.436	24.60	27.71	26.22	24.22	-4.99 ± 1.402	±0.194	±0.285
150.27798	2.827	24.60	26.67	25.00	23.52	-4.99 ± 0.008	±0.081	±0.135
150.37266	2.595	24.14	24.39	23.82	23.83	-2.55 ± 0.259	±0.056	±0.088
149.75593	2.646	23.68	24.67	24.39	23.00	-4.99 ± 0.002	±0.057	±0.108
150.40357	2.824	24.71	24.74	23.66	22.90	-2.56 ± 0.280	±0.042	±0.100
150.40784	1.727	24.72	24.84	23.98	23.53	-2.50 ± 0.290	±0.054	±0.094
150.05048	1.695	24.47	26.02	24.90	23.44	-4.99 ± 0.013	±0.085	±0.191
150.12769	1.713	24.75	24.24	23.33	22.82	-1.15 ± 0.207	±0.037	±0.102
149.65725	1.846	24.32	24.49	23.12	22.21	-2.63 ± 0.317	±0.030	±0.122
149.76969	2.582	24.27	24.17	23.29	22.65	-2.34 ± 0.337	±0.035	±0.138
149.93224	1.641	23.58	23.73	23.05	22.72	-2.73 ± 0.232	±0.034	±0.080
150.5411	2.612	24.43	24.48	23.83	23.41	-2.72 ± 0.355	±0.050	±0.134
149.50626	2.030	23.80	26.40	24.27	22.80	-4.99 ± 0.008	±0.051	±0.179
150.651	1.722	24.36	24.19	23.33	22.96	-1.66 ± 0.195	±0.038	±0.068
149.89718	2.365	24.46	24.56	23.47	22.96	-2.08 ± 0.252	±0.039	±0.095
149.48802	1.924	24.47	26.44	24.73	23.53	-4.94 ± 0.042	±0.074	±0.165

**Table A.1:** A summary of the RA, DEC, magnitudes in different filters and [Fe/H] values with errors for the 165 metal poor candidates

RA	DEC	NB392	$u$	$g$	$i$	[Fe/H]	$\sigma_x$	$\sigma_y$
150.097	2.527	24.23	24.38	23.29	22.59	-2.74 ± 0.213	±0.034	±0.072
149.56522	1.927	24.99	25.01	23.77	22.87	-2.57 ± 0.525	±0.043	±0.221
150.06105	2.227	24.46	24.20	23.50	22.92	-2.30 ± 0.216	±0.039	±0.073
149.6625	1.918	23.86	24.12	22.99	22.56	-2.28 ± 0.233	±0.032	±0.086
150.00285	2.101	23.62	23.78	23.15	22.79	-2.94 ± 0.173	±0.034	±0.053
150.45092	2.617	24.57	24.61	23.72	23.10	-2.73 ± 0.289	±0.044	±0.099
150.152	2.051	24.34	24.39	23.64	23.05	-2.94 ± 0.243	±0.041	±0.080
150.2491	2.418	24.30	24.17	23.40	22.86	-2.30 ± 0.218	±0.037	±0.077
150.55617	2.166	24.85	24.52	23.45	22.93	-1.17 ± 0.217	±0.039	±0.102
150.62203	2.110	24.32	24.51	22.92	22.03	-2.05 ± 0.190	±0.028	±0.069
150.6747	1.716	24.84	24.72	23.24	22.27	-1.89 ± 0.217	±0.033	±0.083
150.18126	2.256	23.52	23.46	22.77	22.30	-2.50 ± 0.145	±0.027	±0.042
150.0678	2.047	24.29	23.72	23.11	23.21	-0.60 ± 0.100	±0.037	±0.072
149.55324	2.258	24.31	26.04	24.39	21.96	-4.99 ± 0.002	±0.055	±0.129
150.17366	2.837	24.21	25.32	23.24	22.03	-3.86 ± 0.161	±0.031	±0.069
150.26953	1.733	24.99	24.71	23.95	23.66	-1.47 ± 0.312	±0.054	±0.130
149.75104	2.323	24.87	24.57	23.18	22.25	-1.56 ± 0.217	±0.033	±0.098
150.25679	2.853	24.33	24.81	23.78	23.09	-3.56 ± 0.232	±0.045	±0.085
149.68281	2.760	23.73	23.98	23.47	23.35	-2.98 ± 0.261	±0.043	±0.092
149.88794	2.492	24.33	24.10	23.24	22.90	-1.47 ± 0.205	±0.035	±0.085
149.87176	2.715	23.81	23.85	22.91	22.26	-2.73 ± 0.248	±0.028	±0.094
150.13148	2.203	24.62	24.51	23.61	22.94	-2.34 ± 0.254	±0.040	±0.081
150.58648	2.389	24.19	24.12	23.06	22.35	-2.15 ± 0.369	±0.030	±0.146
149.75572	2.485	24.37	23.69	22.70	22.14	-0.78 ± 0.127	±0.027	±0.082
150.19071	1.981	24.84	25.44	24.22	23.17	-4.11 ± 0.221	±0.051	±0.116
150.34834	1.963	24.88	25.07	23.67	23.01	-1.92 ± 0.268	±0.042	±0.109
150.50652	2.397	24.80	27.79	26.16	24.71	-4.99 ± 0.003	±0.180	±0.347
150.62128	2.226	23.52	24.40	23.28	22.55	-4.22 ± 0.139	±0.034	±0.077
150.09665	2.196	24.71	25.26	24.51	24.02	-3.91 ± 0.256	±0.068	±0.110
149.97815	2.387	24.27	24.29	23.06	22.56	-1.50 ± 0.187	±0.031	±0.072

**Table A.2:** A summary of the RA, DEC, magnitudes in different filters and [Fe/H] values with errors for the 165 metal poor candidates cont.

RA	DEC	NB392	$u$	$g$	$i$	[Fe/H]	$\sigma_x$	$\sigma_y$
149.80615	2.523	24.72	26.75	24.94	23.13	-4.99 ± 0.004	±0.075	±0.145
149.81083	2.295	24.39	24.33	23.38	22.64	-2.56 ± 0.224	±0.036	±0.073
150.47764	2.120	24.24	23.96	23.10	22.56	-1.70 ± 0.192	±0.032	±0.070
149.94828	2.058	23.84	24.02	23.12	22.64	-2.72 ± 0.180	±0.032	±0.056
149.62959	1.951	24.39	26.10	24.41	23.3	-4.87 ± 0.076	±0.057	±0.144
150.63222	1.769	23.51	23.20	22.56	22.27	-1.66 ± 0.134	±0.027	±0.043
149.78136	2.369	24.44	24.02	23.02	22.36	-1.55 ± 0.204	±0.031	±0.089
150.61047	1.783	24.67	24.04	22.79	21.98	-1.04 ± 0.135	±0.027	±0.071
150.13916	2.299	24.97	24.57	23.50	22.78	-1.57 ± 0.227	±0.038	±0.099
149.8598	1.865	24.55	24.93	23.68	22.99	-2.75 ± 0.362	±0.043	±0.137
150.37562	1.780	24.31	24.22	23.19	22.63	-1.89 ± 0.175	±0.033	±0.062
149.87517	2.111	24.43	24.37	23.89	23.32	-3.35 ± 0.243	±0.048	±0.085
150.11498	2.090	23.97	23.98	23.39	22.75	-3.36 ± 0.185	±0.038	±0.065
149.86953	2.270	24.58	24.72	22.67	22.30	-0.29 ± 0.067	±0.026	±0.075
149.86153	2.509	24.15	23.99	22.95	22.30	-1.92 ± 0.201	±0.029	±0.072
149.97721	2.017	24.56	24.42	23.38	22.63	-2.26 ± 0.236	±0.035	±0.086
149.78503	2.373	24.70	25.60	25.62	23.31	-4.99 ± 0.000	±0.121	±0.197
149.79751	1.818	24.36	26.74	24.83	22.46	-4.99 ± 0.001	±0.071	±0.144
149.45079	2.229	23.57	23.38	22.62	22.23	-1.86 ± 0.162	±0.026	±0.062
150.21054	2.634	24.87	24.66	23.53	22.86	-1.73 ± 0.281	±0.039	±0.118
149.64107	2.789	23.35	23.47	22.88	22.64	-2.74 ± 0.194	±0.030	±0.066
150.29616	2.028	24.54	24.58	23.52	22.71	-2.78 ± 0.252	±0.038	±0.086
150.19868	2.772	23.63	23.64	22.77	22.21	-2.51 ± 0.155	±0.027	±0.049
149.88051	1.926	24.20	25.83	24.34	23.11	-4.93 ± 0.035	±0.056	±0.119
149.89505	2.141	23.93	23.83	22.90	22.21	-2.34 ± 0.167	±0.028	±0.052
150.35906	1.867	23.57	23.76	22.60	22.61	-1.00 ± 0.106	±0.028	±0.047
150.28419	2.227	23.61	23.68	22.84	22.49	-2.28 ± 0.151	±0.029	±0.044
150.66597	2.549	24.01	24.61	23.10	22.29	-3.00 ± 0.245	±0.031	±0.090
150.22779	1.837	24.11	23.83	23.13	22.66	-2.07 ± 0.203	±0.033	±0.069
150.50571	1.979	24.14	24.26	23.34	22.75	-2.73 ± 0.216	±0.036	±0.068

**Table A.3:** A summary of the RA, DEC, magnitudes in different filters and [Fe/H] values with errors for the 165 metal poor candidates cont.

RA	DEC	NB392	$u$	$g$	$i$	[Fe/H]	$\sigma_x$	$\sigma_y$
150.00135	2.534	24.26	24.23	23.20	22.38	-2.78 ± 0.216	±0.032	±0.072
150.2633	2.072	24.36	24.52	23.24	22.47	-2.36 ± 0.217	±0.033	±0.074
149.79153	1.636	24.48	27.46	26.31	23.44	-4.99 ± 0.000	±0.182	±0.298
150.64315	2.473	23.08	23.46	22.66	22.31	-3.15 ± 0.180	±0.027	±0.061
150.43793	2.048	24.93	24.82	23.44	22.57	-1.84 ± 0.264	±0.036	±0.105
149.92568	1.965	23.87	24.07	23.00	22.34	-2.74 ± 0.227	±0.030	±0.077
149.70248	1.955	24.42	24.35	23.21	22.36	-2.41 ± 0.330	±0.032	±0.133
150.03676	1.708	24.59	27.80	25.60	23.46	-4.99 ± 0.000	±0.124	±0.242
150.26677	2.801	23.64	23.22	21.98	21.09	-1.50 ± 0.111	±0.018	±0.042
150.4571	2.068	23.79	23.42	22.62	22.18	-1.48 ± 0.140	±0.026	±0.052
149.58204	1.913	23.15	23.37	22.6	22.11	-3.15 ± 0.154	±0.025	±0.051
150.23	2.643	24.63	24.38	23.34	22.65	-1.75 ± 0.246	±0.035	±0.097
150.6407	2.342	24.27	24.30	23.49	22.99	-2.51 ± 0.360	±0.041	±0.133
150.12264	1.814	24.30	24.57	23.63	23.05	-2.95 ± 0.240	±0.042	±0.083
149.63716	2.380	24.76	24.91	23.68	23.07	-2.10 ± 0.315	±0.043	±0.120
150.50379	2.157	24.35	23.70	23.03	22.54	-1.32 ± 0.178	±0.032	±0.073
150.00518	2.193	24.71	24.56	24.57	24.16	-3.74 ± 0.285	±0.072	±0.115
150.40138	2.218	23.67	23.58	22.57	22.07	-1.69 ± 0.205	±0.024	±0.078
150.41855	2.693	24.02	23.86	22.89	22.24	-2.12 ± 0.185	±0.028	±0.062
150.67335	1.775	23.89	23.47	22.76	22.33	-1.48 ± 0.138	±0.028	±0.049
150.3778	1.698	22.07	21.84	21.46	22.01	-0.95 ± 0.053	±0.019	±0.024
150.30601	2.484	24.07	24.25	23.48	22.93	-3.15 ± 0.208	±0.039	±0.071
150.03622	2.136	23.75	23.67	22.74	21.99	-2.56 ± 0.163	±0.025	±0.048
150.02055	2.237	23.65	23.49	22.62	22.07	-2.09 ± 0.132	±0.025	±0.041
150.56291	2.259	24.44	24.79	23.52	22.72	-2.99 ± 0.396	±0.039	±0.152
150.2603	1.932	23.98	23.98	22.8	22.06	-2.15 ± 0.172	±0.026	±0.060
150.46142	2.129	24.64	23.92	22.93	22.30	-0.92 ± 0.152	±0.029	±0.085
150.50651	1.741	24.58	24.23	23.15	22.46	-1.57 ± 0.177	±0.033	±0.070
149.68513	1.941	23.69	23.65	22.02	20.89	-2.16 ± 0.164	±0.017	±0.069
150.57576	1.636	24.47	24.20	23.08	22.37	-1.75 ± 0.173	±0.031	±0.066

**Table A.4:** A summary of the RA, DEC, magnitudes in different filters and [Fe/H] values with errors for the 165 metal poor candidates cont.

RA	DEC	NB392	$u$	$g$	$i$	[Fe/H]	$\sigma_x$	$\sigma_y$
150.33044	1.897	24.53	24.56	22.93	22.00	-1.87 ± 0.193	±0.027	±0.078
150.17306	2.583	22.90	22.87	22.29	22.51	-1.41 ± 0.096	±0.025	±0.036
149.46864	2.518	23.67	23.55	22.63	22.02	-2.10 ± 0.168	±0.025	±0.054
149.84598	2.445	24.52	24.03	23.05	22.43	-1.22 ± 0.198	±0.031	±0.094
149.85625	2.517	24.32	24.64	23.81	23.41	-2.94 ± 0.285	±0.048	±0.094
149.50241	2.658	24.96	28.25	24.71	22.51	-4.98 ± 0.007	±0.065	±0.167
150.0625	2.032	23.44	23.55	22.85	22.27	-3.15 ± 0.143	±0.028	±0.044
150.15886	2.862	24.77	24.81	23.37	22.31	-2.51 ± 0.265	±0.034	±0.100
149.48916	2.568	24.98	28.02	26.17	23.15	-4.99 ± 0.001	±0.165	±0.273
150.18832	1.858	24.60	27.67	25.77	23.17	-4.99 ± 0.000	±0.130	±0.199
150.39335	2.645	24.56	24.02	22.09	20.76	-1.23 ± 0.139	±0.017	±0.084
149.49674	2.051	24.37	26.71	24.73	23.23	-4.99 ± 0.022	±0.067	±0.292
150.0014	2.005	23.69	23.72	22.97	22.59	-2.50 ± 0.166	±0.031	±0.051
149.86779	1.693	24.20	26.68	26.23	24.17	-4.99 ± 2.520	±0.181	±0.278
150.18473	2.818	24.90	25.19	24.57	22.87	-4.94 ± 0.033	±0.060	±0.130
150.32814	2.468	24.25	27.64	25.13	22.25	-4.99 ± 0.002	±0.082	±0.188
150.43948	2.691	23.76	23.64	23.21	22.58	-3.36 ± 0.178	±0.036	±0.061
150.54233	2.433	23.47	23.27	22.69	22.86	-1.19 ± 0.170	±0.031	±0.082
150.46642	2.164	24.76	26.02	25.40	23.51	-4.99 ± 0.000	±0.106	±0.168
149.97496	2.446	24.46	24.56	22.5	20.44	-3.71 ± 0.143	±0.020	±0.076
150.42255	1.790	24.76	25.39	24.91	23.48	-4.97 ± 0.023	±0.082	±0.130
149.83244	2.001	24.72	24.61	23.38	22.44	-2.43 ± 0.240	±0.034	±0.089
150.38461	2.243	24.00	25.38	23.49	21.63	-4.94 ± 0.024	±0.033	±0.106
149.7579	2.087	23.79	23.62	22.81	22.11	-2.54 ± 0.159	±0.027	±0.048
150.38212	1.870	24.76	24.55	23.28	22.40	-1.87 ± 0.246	±0.033	±0.095
149.82576	1.950	23.91	24.03	22.79	22.05	-2.35 ± 0.223	±0.027	±0.078
150.03696	1.700	24.00	25.19	23.33	22.36	-3.96 ± 0.225	±0.034	±0.108
150.13459	2.853	24.57	24.24	24.07	23.99	-2.30 ± 0.305	±0.062	±0.107
150.22362	2.484	24.11	24.04	22.82	21.98	-2.19 ± 0.176	±0.026	±0.062
150.03425	2.039	23.94	24.07	23.00	22.29	-2.75 ± 0.177	±0.029	±0.056

**Table A.5:** A summary of the RA, DEC, magnitudes in different filters and [Fe/H] values with errors for the 165 metal poor candidates cont.

RA	DEC	$NB392$	$u$	$g$	$i$	[Fe/H]	$\sigma_x$	$\sigma_y$
150.11465	2.061	24.31	24.21	23.03	22.19	$-2.19 \pm 0.204$	$\pm 0.029$	$\pm 0.069$
150.47956	1.736	24.03	23.73	22.70	22.15	$-1.34 \pm 0.130$	$\pm 0.026$	$\pm 0.050$
150.17997	2.707	24.39	24.18	22.97	22.07	$-2.21 \pm 0.203$	$\pm 0.028$	$\pm 0.078$
150.6407	2.093	24.71	24.23	23.12	22.52	$-1.04 \pm 0.172$	$\pm 0.032$	$\pm 0.091$
150.1403	2.124	23.36	23.51	22.82	22.40	$-2.94 \pm 0.149$	$\pm 0.028$	$\pm 0.044$
149.52158	2.331	24.56	27.02	25.95	24.27	$-4.99 \pm 0.000$	$\pm 0.149$	$\pm 0.242$
150.26882	1.819	24.91	24.90	23.37	22.44	$-1.89 \pm 0.272$	$\pm 0.035$	$\pm 0.111$
150.49149	2.367	24.39	27.15	25.09	23.58	$-4.99 \pm 0.003$	$\pm 0.087$	$\pm 0.206$
150.22209	2.141	23.28	23.50	22.57	22.06	$-2.72 \pm 0.138$	$\pm 0.025$	$\pm 0.039$
149.78272	2.197	24.73	24.39	23.40	22.66	$-1.94 \pm 0.227$	$\pm 0.036$	$\pm 0.090$
150.58111	1.622	24.29	23.79	23.00	22.35	$-1.73 \pm 0.173$	$\pm 0.031$	$\pm 0.061$
150.36767	2.670	23.68	23.54	22.75	22.33	$-1.87 \pm 0.159$	$\pm 0.027$	$\pm 0.051$
149.77216	2.023	24.43	24.30	22.37	20.71	$-2.83 \pm 0.156$	$\pm 0.019$	$\pm 0.064$
150.34492	2.279	24.13	23.86	22.90	22.21	$-1.94 \pm 0.273$	$\pm 0.028$	$\pm 0.114$
149.83745	2.182	23.59	23.69	23.27	23.08	$-2.96 \pm 0.181$	$\pm 0.038$	$\pm 0.054$

**Table A.6:** A summary of the RA, DEC, magnitudes in different filters and [Fe/H] values with errors for the 165 metal poor candidates cont.

# References

- Abel T., Bryan G. L., Norman M. L., 2002, *Science*, 295, 93
- Airey J., Eriksson U., 2019, *Designs for Learning*, 11, 99
- An D., Beers T. C., Santucci R. M., Carollo D., Placco V. M., Lee Y. S., Rossi S., 2015, *ApJL*, 813, L28
- Andersen J., 1991, *AAPR*, 3, 91
- Beers T. C., Christlieb N., 2005, *A&A*, 43, 531
- Beers T. C., Preston G. W., Shectman S. A., 1985, *AJ*, 90, 2089
- Beers T. C., Preston G. W., Shectman S. A., Kage J. A., 1990, *AJ*, 100, 849
- Bekki K., Chiba M., 2001, *ApJ*, 558, 666
- Bell E. F., et al., 2008, *ApJ*, 680, 295
- Bertin E., Arnouts S., 1996, *aaps*, 117, 393
- Bond H. E., 1970, *ApJs*, 22, 117
- Bovy J., 2017, *MNRAS*, 470, 1360
- Bromm V., Coppi P. S., Larson R. B., 2002, *ApJ*, 564, 23
- CSIRO A. T. N. F., 2022, Main sequence stars, [https://www.atnf.csiro.au/outreach/education/senior/astrophysics/stellarevolution\\_mainsequence.html#:~:text=Lifespans%20for%20main%20sequence%20stars,years%20on%20the%20main%20sequence.](https://www.atnf.csiro.au/outreach/education/senior/astrophysics/stellarevolution_mainsequence.html#:~:text=Lifespans%20for%20main%20sequence%20stars,years%20on%20the%20main%20sequence.)

- 
- Caputo F., 1998, AAPR, 9, 33
- Carney B. W., Peterson R. C., 1981, ApJ, 245, 238
- Cayrel de Strobel G., 1966, in Loden K., Loden L. O., Sinnerstad U., eds, Vol. 24, Spectral Classification and Multicolour Photometry. p. 350
- Chabrier G., 2003, ApJL, 586, L133
- Chamberlain J. W., Aller L. H., 1951, ApJ, 114, 52
- Christlieb N., Reimers D., Wisotzki L., 2004, The Messenger, 117, 40
- Christlieb N., Schörck T., Frebel A., Beers T. C., Wisotzki L., Reimers D., 2008, AAP, 484, 721
- Clark P. C., Glover S. C. O., Klessen R. S., 2008, ApJ, 672, 757
- Clark P. C., Glover S. C. O., Klessen R. S., Bromm V., 2011, ApJ, 727, 110
- Commons W., 2022, Fraunhofer lines, [https://en.wikipedia.org/wiki/Fraunhofer\\_lines#/media/File:Fraunhofer\\_lines.svg](https://en.wikipedia.org/wiki/Fraunhofer_lines#/media/File:Fraunhofer_lines.svg)
- Deason A. J., Belokurov V., Sanders J. L., 2019, MNRAS, 490, 3426
- Eker Z., Soyduğan F., Bilir S., Bakış V., 2021, MNRAS, 507, 3583
- Fenner Y., Gibson B. K., 2003, pasa, 20, 189
- Frebel A., 2010, Astronomische Nachrichten, 331, 474
- Frebel A., Norris J. E., 2015, A&A, 53, 631
- Frebel A., et al., 2005, Nature, 434, 871
- Gamow G., 1948, Nature, 162, 816
- Giridhar S., 2010, in Principles and Perspectives in Cosmochemistry. p. 165 (arXiv:1003.4002), doi:10.1007/978-3-642-10352-0\_3

- 
- Gotame R. C., 2020, <https://physicsfeed.com/post/harvard-spectral-classification/>
- Greener M. J., Merrifield M., Aragón-Salamanca A., Peterken T., Andrews B., Lane R. R., 2021, MNRAS, 502, L95
- Ishigaki M. N., Tominaga N., Kobayashi C., Nomoto K., 2018, ApJ, 857, 46
- Jenkins A., Wragg F., Butterworth J., Edwards J., O'Neill C., Gough J., Sobral D., 2019, The discovery, abundances and [Fe/H]NB392 distributions of metal-poor stars in the halo of the milky way, <https://eprints.lancs.ac.uk/id/eprint/134675/>
- Johnston S. A., 2022, Betelgeuse and Antares have been observed for over 2,000 years. astronomers can use this to figure out how old they are, <https://www.universetoday.com/156786/betelgeuse-and-antares-have-been-observed-for-over-2000-years-astronomers-can->
- Joye W. A., Mandel E., 2003, in Payne H. E., Jędrzejewski R. I., Hook R. N., eds, Astronomical Society of the Pacific Conference Series Vol. 295, Astronomical Data Analysis Software and Systems XII. p. 489
- Kaler J., 2011, Stars and Their Spectra: An Introduction to the Spectral Sequence. Stars and Their Spectra: An Introduction to the Spectral Sequence, Cambridge University Press, <https://books.google.co.uk/books?id=ZEK02pzuRHoC>
- Karaali S., Bilir S., Gökçe E. Y., 2012, Publications of the Astronomical Society of Australia, 29, 509
- Kardaras I., Kallery M., 2020, Physics Education, 55, 045010
- Keller S. C., et al., 2014, Nature, 506, 463
- Klessen R. S., Glover S. C. O., Clark P. C., 2012, MNRAS, 421, 3217
- Komiya Y., Suda T., Fujimoto M. Y., 2016, ApJ, 820, 59

- Latif M. A., Whalen D., Khochfar S., 2022, *ApJ*, 925, 28
- Libretexts C., 2022, 1.1: Blackbody radiation cannot be explained classically, [https://chem.libretexts.org/Bookshelves/Physical\\_and\\_Theoretical\\_Chemistry\\_Textbook\\_Maps/Physical\\_Chemistry\\_\(LibreTexts\)/01%3A\\_The\\_Dawn\\_of\\_the\\_Quantum\\_Theory/1.01%3A\\_Blackbody\\_Radiation\\_Cannot\\_Be\\_Explained\\_Classically](https://chem.libretexts.org/Bookshelves/Physical_and_Theoretical_Chemistry_Textbook_Maps/Physical_Chemistry_(LibreTexts)/01%3A_The_Dawn_of_the_Quantum_Theory/1.01%3A_Blackbody_Radiation_Cannot_Be_Explained_Classically)
- Magg M., Klessen R. S., Glover S. C. O., Li H., 2019, *MNRAS*, 487, 486
- Miller C. J., 2007, in Graham M. J., Fitzpatrick M. J., McGlynn T. A., eds, *Astronomical Society of the Pacific Conference Series Vol. 382, The National Virtual Observatory: Tools and Techniques for Astronomical Research*. p. 19
- Norris J. E., Peterson R. C., Beers T. C., 1993, *ApJ*, 415, 797
- Osorio Y., Aguado D. S., Prieto C. A., Hubeny I., González Hernández J. I., 2022, *ApJ*, 928, 173
- Palacios A., Gebran M., Josselin E., Martins F., Plez B., Belmas M., Lèbre A., 2010, *AAP*, 516, A13
- Prantzos N., 2008, *A&A*, 489, 525
- Prochaska J. X., Howk J. C., Wolfe A. M., 2003, *Nature*, 423, 57
- Rodrigo C., Solano E., Bayo A., 2012, *IVOA*, p. 1015
- Salpeter E. E., 1955, *ApJ*, 121, 161
- Schneider R., Omukai K., Inoue A. K., Ferrara A., 2006, *MNRAS*, 369, 1437
- Scoville N., et al., 2007, *The Astrophysical Journal Supplement Series*, 172, 1
- Shapiro A. I., Solanki S. K., Krivova N. A., Tagirov R. V., Schmutz W. K., 2015, *AAP*, 581, A116
- Sobral D., et al., 2017, *MNRAS*, 466, 1242
- Stacy A., Bromm V., 2014, *ApJ*, 785, 73

- Stacy A., Bromm V., Lee A. T., 2016, MNRAS, 462, 1307
- Starkenburg E., et al., 2017, MNRAS, 471, 2587
- Wang J., Zhong Z., 2018, AAP, 619, L1
- Wisotzki L., Koehler T., Groote D., Reimers D., 1996, AAPS, 115, 227
- Yanny B., et al., 2009, AJ, 137, 4377
- York D. G., et al., 2000, AJ, 120, 1579
- Yoshida N., Omukai K., Hernquist L., 2008, Science, 321, 669
- Youakim K., et al., 2017, MNRAS, 472, 2963
- Zeilik M., Gregory S., 1998, Introductory Astronomy & Astrophysics. Saunders golden sunburst series, Saunders College Pub., <https://books.google.co.uk/books?id=iH7vAAAAAMAAJ>
- Zhu G., Ménard B., 2013, ApJ, 773, 16